JGR Atmospheres

RESEARCH ARTICLE
10.1029/2022JD037472

Key Points:

- A new version of the NOAA Center for Satellite Applications and Research (STAR) mid-tropospheric layer temperature time series was developed
- Instrument recalibration has removed spurious warming drifts in observations from NOAA-11 to NOAA-14 and spurious cooling drifts in NOAA-15
- The new record yields a trend of 0.14 K/decade during 1979–2021 with an even greater rate of warming after the year 2002 (0.22 K/decade)

Supporting Information:

Supporting Information may be found in the online version of this article.

Correspondence to:

C.-Z. Zou,
Cheng-Zhi.Zou@noaa.gov

Citation:

Zou, C.-Z., Xu, H., Hao, X., & Liu, Q. (2023). Mid-tropospheric layer temperature record derived from satellite microwave sounder observations with backward merging approach. *Journal of Geophysical Research: Atmospheres*, *128*, e2022JD037472. https://doi.org/10.1029/2022JD037472

Received 11 JUL 2022
Accepted 25 FEB 2023

Author Contributions:

Conceptualization: Cheng-Zhi Zou
Formal analysis: Cheng-Zhi Zou, Hui Xu, Xianjun Hao, Qian Liu
Funding acquisition: Cheng-Zhi Zou
Investigation: Cheng-Zhi Zou, Xianjun Hao, Qian Liu
Methodology: Cheng-Zhi Zou, Hui Xu, Xianjun Hao
Project Administration: Cheng-Zhi Zou

Mid-Tropospheric Layer Temperature Record Derived From Satellite Microwave Sounder Observations With Backward Merging Approach

Cheng-Zhi Zou[1], Hui Xu[2], Xianjun Hao[3], and Qian Liu[3]

[1]Center for Satellite Applications and Research, NOAA/NESDIS, College Park, MD, USA, [2]ESSIC/CISESS, University of Maryland, College Park, MD, USA, [3]Environmental Science and Technology Center, College of Science, George Mason University, Fairfax, VA, USA

Abstract We present a new version (v5.0) of the NOAA Center for Satellite Applications and Research (STAR) mid-tropospheric temperature (TMT) time series. This data set uses a backward-merging approach to intercalibrate 16 satellite-based microwave sounding records. The instrument observations included those from the Microwave Sounding Unit (MSU) during 1979–2004, Advanced Microwave Sounding Unit-A (AMSU-A) during 1998–2017, and Advanced Technology Microwave Sounder (ATMS) from 2011 to present. A TMT time series during 2002–present based on satellite microwave observations in stable sun-synchronous orbits was used as a reference in the backward merging process in which earlier satellites were adjusted and merged to the reference. Observations from earlier satellites were recalibrated to remove their calibration drifting errors relative to the reference using sequential overlapping observations. This included removal of spurious warming drifts in the MSU observations onboard NOAA-11, NOAA-12, and NOAA-14 and a spurious cooling drift in the NOAA-15 AMSU-A observations. Temperature changes resulting from diurnal sampling drifts were corrected using an observation-based semi-physical model developed in this study. Other adjustments included channel frequency differences between MSU and AMSU-A companion channels and instrument blackbody warm target effect on observed radiances. These adjustments resulted in inter-consistent TMT records spanning MSU, AMSU-A, and ATMS. The merged time series produced a global mean TMT trend of 0.092 ± 0.043 K/decade during 1979–2021 and a total tropospheric trend of 0.142 ± 0.045 K/decade after removal of a stratospheric cooling effect in TMT. Remarkably, the total tropospheric trends during the latest half period were nearly doubled the earlier half period over the global ocean.

Plain Language Summary Long-term observations of global atmospheric temperatures from satellite microwave sounders play a vital role in climate change research. These observations involved multiple satellites spanning several decades. Careful intersatellite calibration and bias correction are needed to derive inter-consistent records from multi-satellite observations for reliable climate change detection. Here we develop a new version of the NOAA Center for Satellite Applications and Research (STAR) mid-tropospheric temperature (TMT) time series for climate trend investigation. The time series includes instrument observations from three generations of satellite microwave sounders from 1979 to present. Intersatellite biases from several error sources were removed or minimized, including instrument degradation, changes in satellite local observation time, and spectral band differences between different generations of microwave sounders, etc. A unique feature in the time series was satellite merging started from the latest backward to the earlier ones. A TMT time series during 2002-present was used as a reference in the backward merging, which was based on satellite microwave sounder observations with fixed local observation time. The reference TMT has a high accuracy in trend detection, allowing intercalibration and trend detection with better accuracy in time series of the entire period from 1979 to present.

1. Introduction

The Microwave Sounding Unit (MSU) onboard NOAA Polar-orbiting Operational Environmental Satellite (POES) series was a Dicke-type, cross-track scanning microwave spectrometer measuring the global temperature profile from the surface to the lower-stratosphere under all-weather conditions, excluding precipitation, during 1979–2006 (Kidwell, 1998). The MSU passively measures upwelling radiances from atmospheric oxygen in four discrete frequency channels between 50 and 60 GHz. The radiance measured by each frequency channel comes

Resources: Cheng-Zhi Zou
Software: Hui Xu, Xianjun Hao, Qian Liu
Visualization: Cheng-Zhi Zou, Hui Xu, Xianjun Hao
Writing – original draft: Cheng-Zhi Zou
Writing – review & editing: Cheng-Zhi Zou, Hui Xu, Xianjun Hao, Qian Liu

from a different layer of the atmosphere, depending on the strength of the absorption at that frequency. The relative contribution of temperatures at individual levels to the measured layer temperature is represented by a vertical weighting function, which is typically a bell-shaped curve peaking at a certain altitude. Since 1998 until present, the Advanced Microwave Sounding Unit-A (AMSU-A) on board NOAA-15 through NOAA-19, NASA Aqua, and European MetOp series have replaced MSU to provide global temperature profile observations with 15 channels and higher vertical and horizontal resolutions (Robel & Graumann, 2014). The Advanced Technology Microwave Sounder (ATMS) being flown on the current Suomi National Polar-orbiting Partnership (SNPP) and the NOAA Joint Polar Satellite System-1 (JPSS-1, renamed NOAA-20 after launch) and to be flown on future JPSS satellites is the third generation of the microwave sounders. ATMS is a total-power cross-track radiometer that has the same channel frequencies as AMSU-A for most temperature sounding channels and will carry the NOAA microwave sounding capability into the future (Goldberg et al., 2013; Weng et al., 2012). Although all these instruments were designed primarily for weather observations, they represent an indispensable long-term global climate data record (CDR) due to the length of the record, insensitivity to clouds, and global coverage.

Three groups, including the NOAA Center for Satellite Applications and Research (STAR; Zou & Wang, 2011; Zou et al., 2006, 2018, 2021), the University of Alabama at Huntsville (UAH; Christy et al., 2003; Spencer & Christy, 1992a; Spencer et al., 2017), and the Remote Sensing Systems (RSS; Mears & Wentz, 2009, 2016; Mears et al., 2003), have developed merged MSU and AMSU-A temperature time series for layers of the mid-troposphere (TMT), upper-troposphere (TUT), and lower-stratosphere (TLS). These time series were based on the near nadir observations from the MSU channels 2, 3, and 4 with central spectral frequencies at 53.74, 54.96, and 57.95 GHz, respectively, merged with their corresponding AMSU-A companion channels. The RSS and UAH groups also developed the lower-tropospheric temperature (TLT) time series using combinations from either different off-nadir observation of MSU channel 2 (Mears & Wentz, 2017; Spencer & Christy, 1992b; Wentz & Schabel, 1998) or different MSU channels (Spencer et al., 2017). In addition, the University of Washington (UW, Po-Chedley et al., 2015) group developed a TMT time series over the tropical region. These data sets had been extensively used to investigate climate trends in atmospheric temperatures during the satellite era (Christy et al., 2003; Fu et al., 2004; Mears et al., 2003; Spencer & Christy, 1992a, 1992b; Steiner et al., 2020; Wentz & Schabel, 1998; Zou & Wang, 2011, Zou et al., 2021). Studies of these temperature data records have enhanced our understanding on a number of climate change topics including human influence on the yearly mean trends and seasonal cycle of tropospheric temperature (Santer et al., 2013, 2018, 2022), tropical expansion (Fu & Lin, 2011; Fu et al., 2006), atmospheric temperature trends over North America (Ohring et al., 2014), strengthening of the Brewer-Dobson circulation (Fu et al., 2015, 2019), variability and trends in the lower-stratospheric temperatures (Seidel et al., 2016), trend differences between climate model simulations and satellite observations (McKitrick & Christy, 2020; Po-Chedley et al., 2021; Randel et al., 2017; Santer, Fyfe, et al., 2017; Santer, Solomon, et al., 2017), and warming amplification in the tropical upper-troposphere (Fu & Johanson, 2005; Fu et al., 2011; Santer et al., 2005; Steiner et al., 2020).

Although rich in applications, residual biases still remain in these data sets after satellite processing which influence MSU-derived long-term trends. One of the main sources of error is from the diurnal sampling differences, which occur when satellites sample Earth at different local times due to their deployment in different sun-synchronous orbits. This problem also afflicts individual satellites as their orbits drift with satellite aging. If not corrected, the temperature diurnal differences due to different observation time can become aliased with the long-term satellite time series, causing spurious trends in the satellite observations (Trenberth & Hurrell, 1997). Different diurnal correction algorithms greatly affect long-term TMT trend estimates (Christy et al., 1998; Mears & Wentz, 2016; Po-Chedley et al., 2015). Another source of error is from the satellite instrument calibration, a process that converts the signals received by the satellite antenna in the form of electric voltage counts to the Earth radiance measurement. Calibration errors may drift over time due to instrument degradation (Zou & Wang, 2011; Zou et al., 2006). For example, NOAA-14 and NOAA-15 exhibited large relative calibration drifts up to 0.2–0.3 K per decade during their overlapping period (Mears & Wentz, 2016). Different decisions on the treatment of this drift affected the trend results over the full time period in the final merged products (Santer et al., 2021). Different TMT data set also produced widely varying ratios of trends between tropical tropospheric temperature and tropical total column water vapor (Santer et al., 2021). In contrast, climate model simulations consistently exhibit a ratio close to 5.5%/K (Santer et al., 2021). These comparisons call for more accurate satellite TMT data sets for reliable trend detection.

The launch of the new generation of microwave sounders, the ATMS onboard the SNPP and NOAA-20 and future JPSS satellite series, brings a few distinct advantages that could potentially improve the accuracy of the atmospheric temperature data products. First, the ATMS temperature-sounding channels have exactly the same channel

frequencies for most channels as its predecessor, the AMSU-A (Goldberg et al., 2013; Weng et al., 2012). This is a critical feature of the instrument design that allows temperature of the same atmospheric layers to be measured continuously from the past to the present and onward to the future (Zou et al., 2014). Second, the ATMS satellites do not have diurnal drift problem because they use onboard propulsion to fix their local equatorial crossing time (LECT) to ~1:30 p.m. on the ascending node (Zou et al., 2018). Third, recent research indicates that observations from the SNPP/ATMS, Aqua/AMSU-A, and MetOp-A/AMSU-A have exhibited high radiometric calibration stability of 0.04 K/decade (Zou et al., 2018). With this high radiometric stability performance, Zou et al. (2021) developed a TMT time series using satellite microwave sounders only in stable sun-synchronous orbits which covers the period from 2002 to present. Such a TMT time series has an accuracy of 0.01 K/decade in trend detection, exceeding the GCOS (2016) stability requirements of 0.02 K/decade. As a result, this time series can be used as a reference measurement for climate variability and atmospheric temperature trends for the period from 2002 to present. It may also be helpful in the development of atmospheric temperature time series with a better accuracy for satellites before the millennium when used as a reference (Zou et al., 2021).

The goal of this study is to develop an upgraded STAR version of the MSU-based TMT time series for the period from late 1978 to present using the reference TMT (abbreviated as RTMT hereafter) developed by Zou et al. (2021) for the period of 2002–present as a reference. The STAR version of the temperature CDR had gone through a series updates over the years. It started from the Version 1 MSU-only data record (Zou & Wang, 2010; Zou et al., 2009) to Version 2 merged MSU and AMSU-A time series (Zou & Wang, 2011). The Version 3 data set was improved by adding more AMSU-A satellites with improved limb adjustment schemes (Zou et al., 2015). Versions 4.0 adopted the diurnal adjustment algorithms developed by Po-Chedley et al. (2015) and the latest Version 4.1 implemented an improved frequency adjustment scheme for the MSU and AMSU-A merging. All of these earlier versions are considered as forward merging as the later AMSU-A observations were adjusted and merged to the earlier MSU observations with the end products represented by the MSU-based weighting functions.

Different from the previous versions, here we apply a new merging strategy in which the RTMT is used as a reference and the merging starts from this reference backward all the way to the earliest MSU observations onboard TIROS-N satellite. The resulting data set, which is named STAR Version 5.0 in the rest of this study, is a data record using the AMSU-A/ATMS weighting functions to represent its measured atmospheric layers. In addition, we recalibrate most satellites used in the data sets to remove or minimize calibration drifting errors and develop a semi-physical model to remove diurnal drifting errors. These recalibration and diurnal adjustments are also conducted backward using RTMT as a reference. We expect the new data set developed with the backward approach to inherit the high accuracy in trend detection in RTMT.

The upgraded version includes TMT, TUT, and TLS products with similar merging approaches, but our description only focuses on TMT here. The next Section describes level-1 radiance data used in the study. In subsequent sections we describe the recalibration method and results (Section 3), the frequency adjustments between MSU and AMSU-A (Section 4), the semi-physical model for diurnal drift adjustment and results (Section 5), and the correction of the warm target effects (Section 6). Section 7 compares the STAR V5.0 with existing data sets. Section 8 discusses trends and their uncertainties in the STAR 5.0 TMT time series. Section 9 contains a conclusion.

2. The Satellite Data Sets Used in This Study

2.1. The Reference TMT Time Series

The monthly RTMT time series developed by Zou et al. (2021) is used as a reference (anchor) in the backward merging processes in our TMT development. RTMT spans the period from August 2002 to present with near-global coverage and a binned resolution of 2.5° × 2.5°. RTMT includes satellite microwave sounder observations from AMSU-A onboard Aqua and MetOp-A and ATMS onboard SNPP and NOAA-20 which are all in stable sun-synchronous orbits. RTMT is an anomaly time series which is accessible through the STAR website: https://www.star.nesdis.noaa.gov/smcd/emb/mscat/products.php. In our application, the monthly climatology averaged from ascending and descending orbits from MetOp-A during January 2008–December 2017 was added to the RTMT anomalies in order to recover the absolute values of the brightness temperature at each grid point. Note that a monthly climatology from ascending or descending only orbits is defined at the ascending or

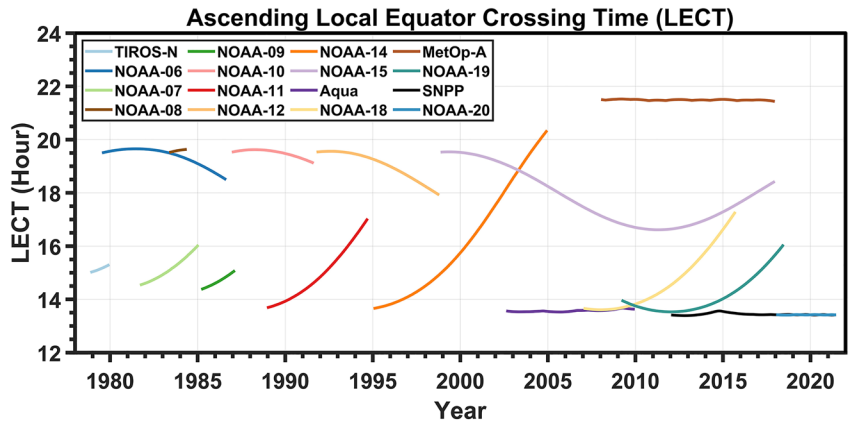

Figure 1. Ascending Local Equator Crossing Time (LECT) for polar-orbiting satellites used in this study. The descending LECT is 12 hr apart from the ascending LECT. Satellites with their descending LECTs near 7:30 a.m. at launch time are referred to as "morning satellites" (NOAA-6, -8, -10, −12, and −15), while satellites with their ascending LECTs around 2:30 p.m. at lunch time are referred to as "afternoon satellites" (TIROS-N, NOAA-7, -9, -11, -14, -18, and -19).

descending local times, while their averages give the recovered RTMT as a monthly mean "daily" time series which is not associated with a specific local time.

2.2. The MSU and AMSU-A Data Sets

The MSU observations derived from nine NOAA POES satellites (TIROS-N to NOAA-14) spanning from November 1978 to December 2004 and the AMSU-A observations followed from MSU over November 1998–June 2018 are used to merge with RTMT to develop the STAR V5.0 TMT. Figure 1 shows the ascending LECT and Table 1 lists the time period spanning for each of these satellites. Satellite level-1c swath radiances or brightness temperatures (TBs) are the basis for developing gridded TMT. Swath TBs for TIROS-N to NOAA-9 were taken from NOAA's National Centers for Environmental Information (NCEI) Climate Data Record Program (https://www.ncei.noaa.gov/products/climate-data-records/fundamental), which was originally produced by the STAR group as an MSU fundamental climate data record (Zou & Wang, 2010; Zou et al., 2009). The swath radiances for MSU satellites from NOAA-10 to NOAA-14 and AMSU-A satellites from NOAA-15 to NOAA-19 are obtained in this study through recalibration of the raw measurements in the form of electric voltage digital counts. The raw counts and other data needed for recalibration were taken from the level-1b data archived in the NOAA Comprehensive Large Array-data Stewardship System (CLASS, https://www.avl.class.noaa.gov/saa/products/welcome). The recalibration used a simultaneous nadir overpass (SNO) method, developed by Zou et al. (2006) and Zou and Wang (2011), to obtain optimal calibration coefficients and minimize inter-satellite differences. A detailed description on the recalibration approach and results is given in Appendix A and Section 3.

Table 1
Time Period for Each Satellite Used in the TMT Development

Satellite/Instrument	Time period
TIROS-N/MSU	11/1978 to 12/1979
NOAA-6/MSU	07/1979 to 03/1983
	05/1985 to 08/1986
NOAA-7/MSU	09/1981 to 02/1985
NOAA-8/MSU	05/1983 to 05/1984
NOAA-9/MSU	03/1985 to 02/1987
NOAA-10/MSU	12/1986 to 08/1991
NOAA-11/MSU	12/1988 to 09/1994
NOAA-12/MSU	10/1991 to 10/1998
NOAA-14/MSU	01/1995 to 12/2004
NOAA-15/AMSU-A	11/1998 to 12/2017
NOAA-18/AMSU-A	01/2007 to 09/2015
NOAA-19/AMSU-A	03/2009 to 06/2018
MetOp-A/AMSU-A	01/2008 to 12/2017
Aqua/AMSU-A	08/2002 to 12/2009
SNPP/ATMS	01/2012 to 06/2021
NOAA-20/ATMS	01/2018 to 06/2021

After the swath radiance data are obtained, a limb-adjustment is conducted in which radiances at off-nadir view angles were adjusted to those at the nadir direction. This adjustment allows the use of the off-nadir footprints in the same way as the nadir observations to increase observational samples and reduce noise and sampling-related biases in TMT. We use Community Radiative Transfer Model (CRTM, Han et al., 2006) simulations to derive the limb-adjustment, which was the CRTM simulated differences for each scan position between those with off-nadir and zero scan angles. The simulations were conducted for each satellite to accommodate their different altitudes and scan positions. The NASA's Modern-Era Retrospective analysis

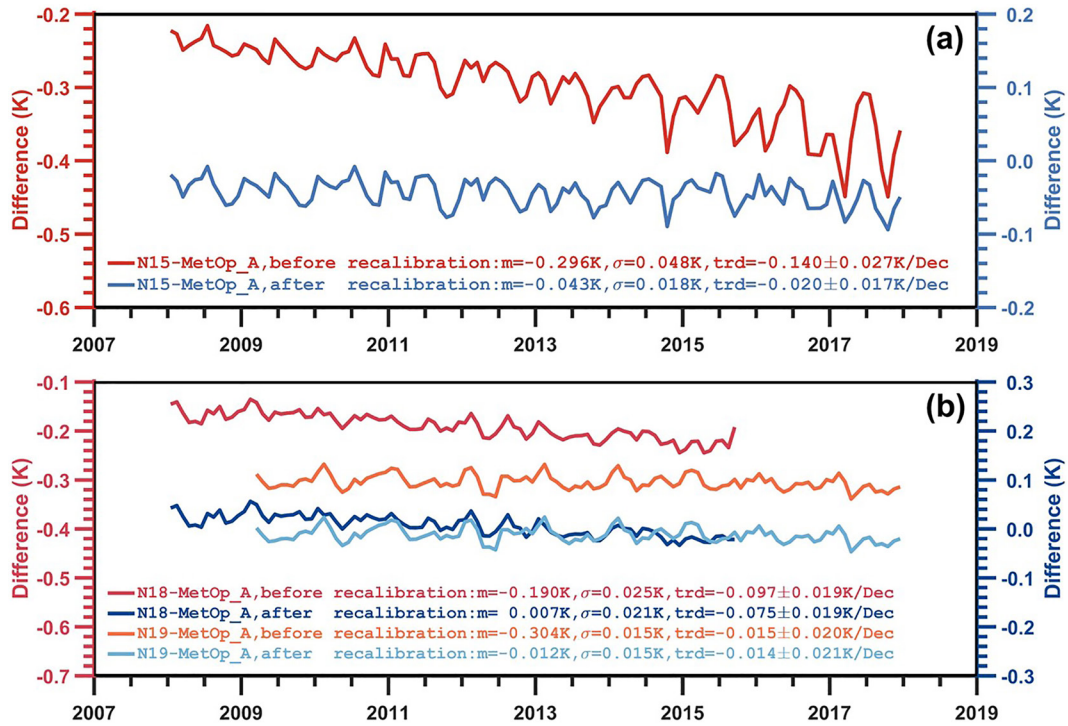

Figure 2. (a) Inter-satellite difference time series of global ocean mean brightness temperatures of AMSU-A channel 5 between NOAA-15 and the reference, MetOp-A, for before and after recalibration in this study; (b) Same as (a) except for differences between NOAA-18 and MetOp-A and between NOAA-19 and MetOp-A. Global ocean means were averages of the ascending and descending orbits. The NOAA-15 and NOAA-18 data before recalibration were from the NCEI CDR archive while the NOAA-19 data was from the CLASS archive.

for Research and Applications, Version 2 (MERRA2, Gelaro et al., 2017) reanalysis was used as inputs to the simulation. Off-nadir biases can be as large as more than 10 K, depending on scan angles, before limb-adjustment (Goldberg et al., 2001; Wang & Zou, 2014). They were reduced to less than 0.1 K for scan positions 8–23 after the limb-adjustment (Wang & Zou, 2014). After the limb-adjustment, monthly gridded data were generated, for ascending and descending orbits separately, by accumulating and binning limb-adjusted TBs into grid cells with a resolution of 2.5° latitude by 2.5° longitude and then averaged in monthly intervals. Each MSU scanline contains 11 fields of view (FOVs); limb-adjusted views from the scan positions 3 to 9 were used in the monthly grid cells. Similarly, each AMSU-A scanline has 30 FOVs. Among them, limb-adjusted views from the scan positions 8 to 23 were used in the monthly gridded products to match with the MSU swath width.

3. Recalibration of AMSU-A and MSU Observations With Backward Approach

3.1. Recalibration of the AMSU-A Observations

NOAA-15, NOAA-18, and NOAA-19 have been operational for more than 20, 15, and 10 years, respectively. There are two existing versions of level-1 AMSU-A data: the swath radiance data from NOAA operational calibration archived in NOAA CLASS and the inter-calibrated level-1c swath radiance data archived in NOAA NCEI CDR program (https://www.ncei.noaa.gov/products/climate-data-records/amsu-brightness-temperature-noaa). Both versions are referred to as data before recalibration, relative to data after recalibration conducted in this study. The AMSU-A data of before recalibration were used in the existing STAR, RSS and UAH TMT times series. Figure 2a shows inter-satellite difference time series of global ocean means between NOAA-15 and MetOp-A before and after their recalibration and Figure 2b shows similar time series but for the satellite pairs between NOAA-18 and MetOp-A and between NOAA-19 and MetOp-A. Here the NOAA-15 and NOAA-18 data before recalibration were from the NCEI CDR archive while the NOAA-19 data was from the CLASS archive. Note that differences of NOAA-15, NOAA-18, and NOAA-19 relative to MetOp-A are nearly identical to their differences relative to RTMT since MetOp-A had been included in RTMT and their relative drifting errors were

small (less than 0.016 K/decade, Zou et al., 2021). As seen in Figure 2a, data quality problems in NOAA-15 manifested as a large non-climate seasonal variability in TBs occurred after 2015 before recalibration. This variability was a residual instrument temperature variability induced by solar-heating differences that showed up in radiances due to inaccurate calibration nonlinearity (see analysis in Appendix A and Zou and Wang (2011)). Large cooling drifts in NOAA-15 and NOAA-18 before recalibration were also found. The large cooling drift in NOAA-15 was also seen in bias correction analyses in the ERA-Interim climate reanalysis (Dee & Uppala, 2009). NOAA-19 was relatively stable compared to MetOp-A, although their inter-satellite biases were up to 0.3 K.

We have recalibrated NOAA-15, NOAA-18, and NOAA-19 in this study using MetOp-A as a reference. The reason for selecting MetOp-A, rather than RTMT, as the reference is that recalibration is conducted at swath level. This requires raw data such as the MetOp-A raw counts as inputs. Since bias drift between MetOp-A and RTMT is small, the recalibration is similar to using RTMT as a reference. In the recalibration, cold space views and internal blackbody warm target views from a radiometer were used to calibrate scene temperatures from the Earth views. Temperature measurements from the cold space and warm target views were assumed to incur drifting errors that vary linearly with time owing to possible degradations in blackbody emissivity, reflector, and/or antenna surface materials. In addition, each instrument was assumed to suffer detector degradation which also varies linearly over time. These instrument degradations caused calibration coefficients, including offsets and calibration nonlinearity, to change linearly over time. The net effects of these changes are an addition of a bias drift to the original scene temperatures that vary approximately linearly with time and reduction of the solar-heating induced seasonal variability in radiances. The SNO method developed by Zou et al. (2006) and Zou and Wang (2011) is used to derive calibration coefficients for NOAA-15, NOAA-18, and NOAA-19 using their long overlaps with MetOp-A. The recalibration procedure, resulting calibration coefficients, and possible mechanisms to explain the recalibration results are described in detail in Appendix A. As seen in Figure 2a, the recalibration significantly reduced the large seasonal variability and the long-term cooling drift found in NOAA-15 before recalibration. The standard deviation and relative trend between NOAA-15 and MetOp-A for their 10-year global ocean mean differences were respectively 0.018 K and −0.02 K/decade after recalibration, in contrast to 0.048 K and −0.14 K/decade before recalibration. These improvements occurred because, by construction, optimal time-varying calibration coefficients were obtained for NOAA-15 to minimize its differences relative to MetOp-A using their overlap observations. In addition, inter-satellite biases between NOAA-19 and MeOp-A were reduced to close to zero by the recalibration. Nevertheless, the cooling drift found in NOAA-18 before recalibration largely remained after recalibration. This was dominated by the diurnal drifting errors and is discussed further in Section 5 shortly.

The recalibrated drift adjustment to NOAA-15 was actually applied to its entire lifecycle from 1998 to 2017, but Figure 2a only showed its recalibration performance from 2008 to 2017, during which its orbit went through a parabolic curve with a total drift for only about 1 hr (Figure 1). This small orbital drift had little impact on the analysis of calibration drift in NOAA-15 relative to MetOp-A. Since NOAA-15 was the only AMSU-A satellite connecting RTMT to the last MSU on NOAA-14, it is desirable to understand its recalibration performance during its earlier operational period. Before MetOp-A, NOAA-15 overlapped with NOAA-14 during 1998–2004 and with Aqua during 2002–2009. During these periods, the NOAA-15 orbit monotonically drifted for about 3 hr from 7:30 p.m. to 4:30 p.m. in ascending node (Figure 1). This orbital drift affects the analysis of its recalibration performance. As such, evaluation of the NOAA-15 recalibration performance during its overlaps with Aqua and NOAA-14 will be discussed in Section 5 together with its diurnal drift adjustment.

3.2. Recalibration of MSU Observations

NOAA-14 carried the last MSU instrument. Its observations were found to drift warmer relative to NOAA-15 in previous studies (e.g., Mears & Wentz, 2016; Spencer et al., 2017). In this study, we have recalibrated NOAA-14, as described in detail in Appendix A, to remove their relative bias drifts using the recalibrated NOAA-15 as a reference. Figure 3a shows difference time series of global ocean means between NOAA-14 and the recalibrated NOAA-15 for before and after NOAA-14 recalibration, respectively. Before recalibration, NOAA-14 drifted warmer relative to NOAA-15 with a magnitude of 0.20 K/decade during their 6-year overlaps from late 1998 to the end of 2004. If compared to non-recalibrated NOAA-15 which had a cooling drift, the warming drift in NOAA-14 would be even larger (not shown). The spurious cooling drift in NOAA-15 and spurious warming drift in NOAA-14 before recalibration had caused an ambiguity in satellite merging. Different decisions on the two satellites, considering either NOAA-15 or NOAA-14 as the truth, had significantly affected trends of the merged

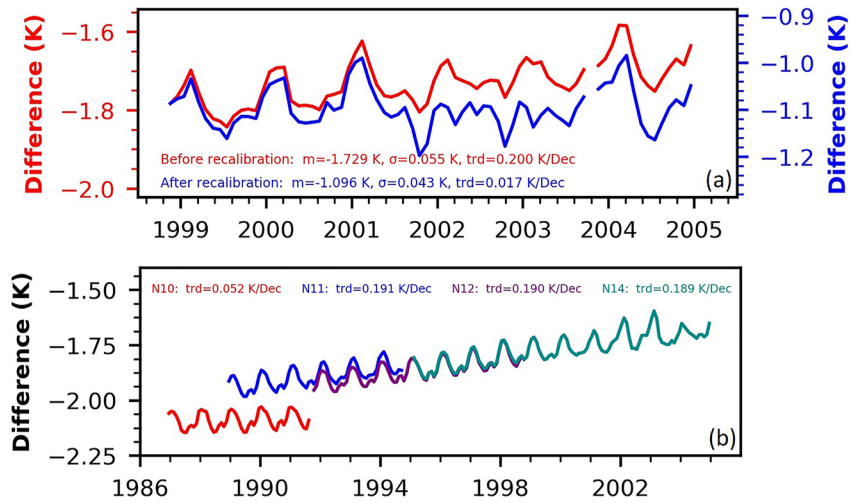

Figure 3. (a) Global ocean mean difference time series of brightness temperatures between the recalibrated NOAA-15 AMSU-A channel 5 and NOAA-14 MSU channel 2 for before (red) and after (blue) recalibration of NOAA-14. Note the mean difference between NOAA-14 and NOAA-15 is still non-zero after the recalibration, due to their channel frequency differences. (b) Global mean differences for before minus after recalibration for NOAA-10 to NOAA-14, showing their spurious warming drifts before recalibration.

TMT time series (Mears & Wentz, 2016; Santer et al., 2021). Here the drift between NOAA-14 and NOAA-15 was reduced to 0.017 K/decade after recalibration (Figure 3a). This is similar to subtracting a linear trend between the two satellites that makes NOAA-14 consistent with NOAA-15 and further with RTMT.

Other MSU observations onboard NOAA-12 to NOAA-10 were also recalibrated sequentially backward using their overlapping observations (the recalibration procedure is discussed in Appendix A). Figure 3b shows their global-mean difference time series between before and after recalibration. These differences exhibited large spurious warming drifts up to 0.19 K/decade for satellites from NOAA-11 to NOAA-14 and a smaller warming drift for NOAA-10 for observations before recalibration. Christy et al. (2018) also found spurious warming drifts in these satellites when compared to radiosonde observations. Large warming drifts in NOAA-11 and NOAA-14 before recalibration were also seen before 2003 in bias correction analyses in ERA-Interim climate reanalysis (Dee & Uppala, 2009). As discussed later on in Section 7, the removal of these bias drifts in our recalibration has significant impact on the resulting trends of the merged TMT time series from late 1978 to present.

4. Frequency Adjustment to the MSU Observations

Due to differences in channel frequencies, MSU channel 2 and AMSU-A channel 5 have slightly different weighting functions and thus measure different layers of the atmosphere at the nadir direction. This results in scene temperature differences because tropospheric temperature decreases with altitude. The varying atmospheric lapse rates over time and space would cause the scene temperature differences to change over time and geolocation. These differences must be removed for the two instrument observations to be merged together for TMT development.

The frequency adjustment in the STAR TMT data included two steps. The first was to derive a first-guess adjustment based on CRTM simulations. Here in two simulations, the CRTM setups were exactly the same except the channel frequency inputs were taken from the AMSU-A channel 5 and MSU channel 2, respectively. The frequency adjustment was taken as the simulated TB differences between the two simulations using NASA MERRA2 reanalysis as inputs. Two types of MERRA2 data, both with a spatial resolution of 0.5° latitude × 0.625° longitude, were used in the simulation: the hourly surface data containing skin temperature and wind vector and 3-hourly atmospheric profiles including temperature, water vapor, ozone, cloud liquid water, and wind vector. The simulation was conducted for six-year MERRA2 data (November 1998–December 2004) during which NOAA-14 overlapped with NOAA-15. This simulation was then converted to a 2.5° × 2.5° gridded climatology for frequency adjustment of all satellites from NOAA-14 to TIROS-N. After the first-guest adjustment, differences between

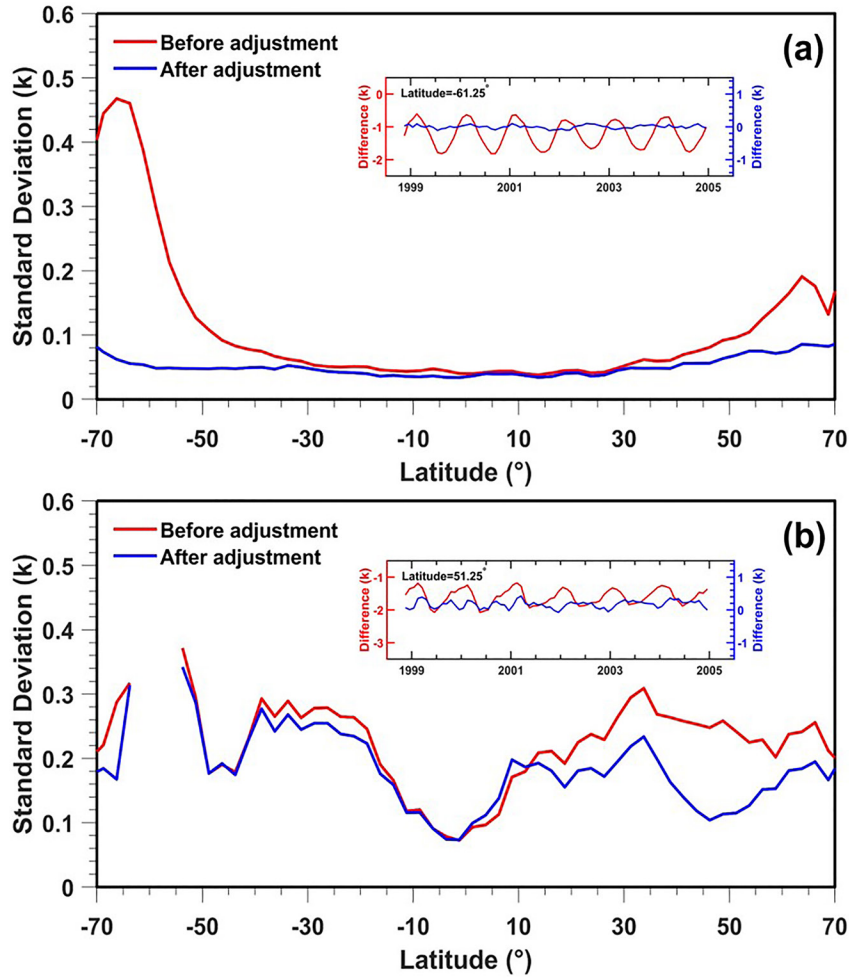

Figure 4. Standard deviations of the zonal mean difference time series between NOAA-14 MSU channel 2 and NOAA-15 AMSU-A channel 5 versus latitudes for (a) over ocean and (b) over land. The red and blue lines represent before and after the frequency adjustment, respectively. The insets show examples of the difference time series before and after the frequency adjustment at near 60°S over the ocean and near 50°N over the land, respectively.

the MSU and AMSU-A may still exist owing to residual calibration errors over the ocean and diurnal differences over land. To remove possible calibration errors and as a second step, the first-guess adjustment was modified by a climatology derived from the differences between NOAA-15 and NOAA-14 over the ocean. This climatology was calculated by averaging the NOAA-15 and NOAA-14 differences for the same month at each grid point through the period from January 1999 to December 2004. These gridded differences were further averaged in latitudinal belts over the ocean to derive a zonal mean climatology which was used to modify and constrain the zonal mean magnitude of the first-guess adjustment so that the latter quantity equals the former for each month and latitude. In this way, the final frequency adjustment term equals the latitudinal climatology over the ocean while adjustments at individual grid points follow lapse rate structures from the CRTM simulations.

The frequency adjustment reduced the means and the amplitudes of seasonal cycles in the NOAA-14 and NOAA-15 difference time series. Figures 4a and 4b show impact of the frequency adjustment on the standard deviations (STDs), representing the seasonal amplitudes of the difference time series between NOAA-14 and NOAA-15 over ocean and land, respectively. The effects of adjustment are quite different over land and ocean, depending on seasonal amplitudes of diurnal differences and changes in the atmospheric lapse rates. In Figure 4a, the seasonal amplitudes in the temperature differences are small over the low-latitude ocean (less than 0.1 K) owing to small diurnal amplitudes and seasonal changes of the atmospheric lapse rate. As a result, the frequency adjustment mainly reduced the mean temperature differences between the two satellites but the seasonal amplitudes remained unchanged over the low-latitude ocean. Over the Northern and Southern high-latitude oceans, the

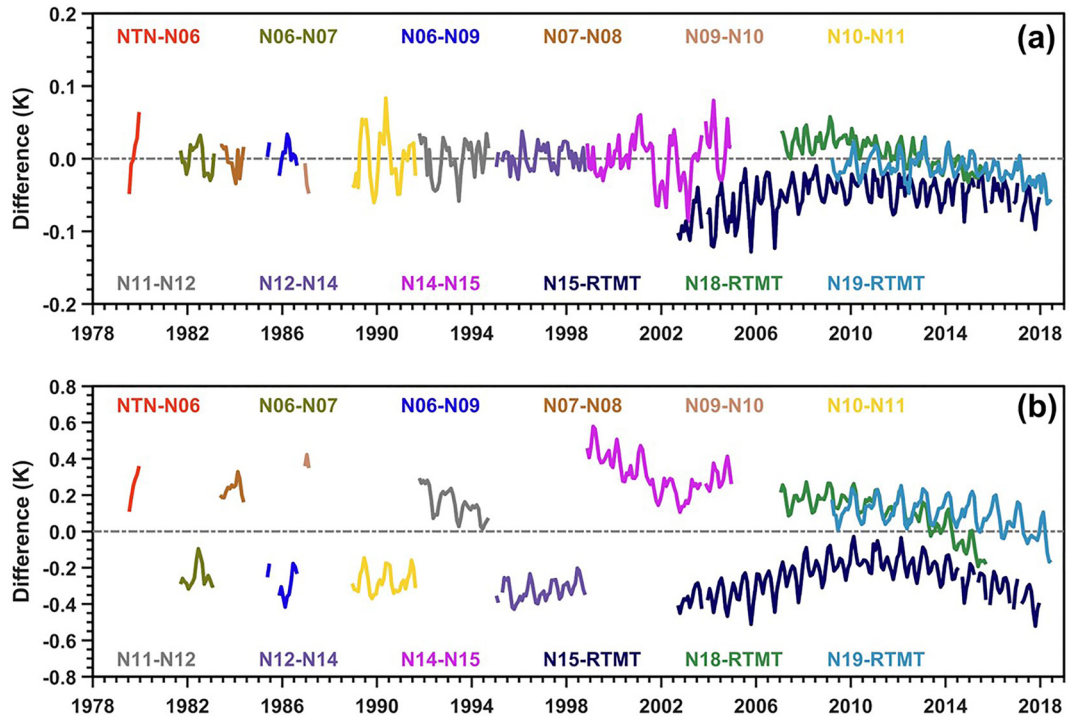

Figure 5. Inter-satellite difference time series for satellite pairs between those from TIROS-N to RTMT after the frequency adjustment for (a) over the global ocean and (b) over the global land.

temperature differences between NOAA-14 and NOAA-15 had large seasonal amplitudes up to 0.2 and 0.4 K, respectively, before the frequency adjustment due to larger seasonal variations in the atmospheric lapse rates. These large differences were reduced to less than 0.1 K after the frequency adjustment, being close to those over the low-latitude oceans. This gives an overall satisfactory frequency adjustment over the ocean.

The frequency adjustments also reduced the seasonal amplitudes in the temperature differences over land, but the reduction was not as large as over the ocean. Over the deep tropics, reduction of the seasonal amplitudes from the frequency adjustment was ignorable since they are already small (less than 0.1 K, Figure 4b). The reduction of the seasonal amplitude increased with increasing latitudes and the maximum reduction occurred near 50°N (Figure 4b). However, the seasonal amplitudes are still on the order of 0.2–0.3 K over most latitudes except over the deep tropics after the frequency adjustment. This is different from the adjustment over the ocean because the seasonal amplitudes of diurnal differences are larger over land.

The frequency adjustments derived from the NOAA-14 and NOAA-15 observations were applied to all the MSU satellites. Figures 5a and 5b show inter-satellite difference time series of global ocean and land means, respectively, for satellite pairs from TIROS-N to RTMT after this adjustment. As seen, the mean differences and bias drifts between satellite pairs are quite small over the ocean, but they are still large over land. These biases are to be reduced by adjustments of diurnal drifts and warm target effects as described in the following two sections.

5. Diurnal Drift Adjustment

The diurnal drift effect is caused by satellite orbital drift that results in changes in local observation time (Figure 1). Biases caused by diurnal drift can be removed by adjusting the scene brightness temperatures at different observation time from all different satellites to a common local time before satellite merging. The diurnal cycle used for such an adjustment is a function of time and geolocation. Mears et al. (2003) used a climate model to simulate a diurnal cycle climatology in order to estimate and remove the effects of diurnal drift. In the latest version of RSS data set, the model simulated diurnal cycles were further modified by observations to derive optimized diurnal adjustment (Mears & Wentz, 2016). Po-Chedley et al. (2015) developed a novel approach where diurnal cycles were represented by a polynomial function of satellite local observation time and the coefficients of the

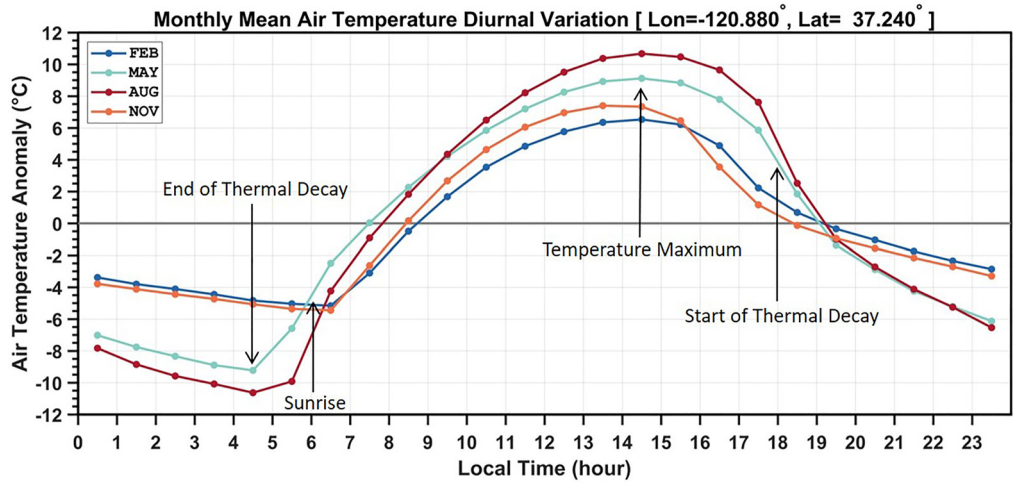

Figure 6. Monthly mean diurnal cycles for the 1.5 m near-surface air temperature at (lon = −120.88°, lat = 37.24°) for selected months. The arrow lines represent approximate times in the May and August diurnal cycles for events indicated by the corresponding texts. The monthly diurnal data was generated using the hourly air temperature data products from the U.S. Climate Reference Network (USCRN, Diamond et al., 2013).

polynomial functions were obtained from inter-satellite differences. Such an observation-based approach effectively removed diurnal drift errors. Here we apply a diurnal adjustment similar to Po-Chedley et al. (2015) but extend it in two ways. First, instead of a polynomial function, we use a semi-physical model of diurnal cycles for the adjustment. Figure 6 shows typical monthly diurnal cycles for near-surface air temperature over land. Atmospheric tidal theory and modeling suggest that daytime atmospheric tides are composed of migrating diurnal and semi-diurnal components owing to absorption of solar radiation by water vapor in the troposphere and ozone in the middle atmosphere (Braswell & Lindzen, 1998; Chapman & Lindzen, 1970; Lindzen, 1967). Absorptions of solar radiation by clouds and latent heating from precipitation may also affect amplitudes and phases of semi-diurnal component of the atmospheric tides (Dai & Wang, 1999; Lindzen, 1978). Sun-following sensible heating from the ground excites nonmigrating diurnal component over land, resulting in much larger diurnal amplitude over land than over the ocean (Dai & Wang, 1999; Haurwitz & Cowley, 1973; Li & Smith, 2010). Atmospheric tides are reflected by diurnal variations in surface pressure and temperature, and also in TMT which contains about 1%–10% contribution from the surface, depending on surface types and incident angles. During nighttime, thermal decay prevails (Figure 6; Duan et al., 2014; Inamdar et al., 2008). Based on the tidal theory, we assume the following mathematical model to represent diurnal anomalies,

$$D(\boldsymbol{X}, m, L_t) = \sum_{i=1}^{2} D_i(\boldsymbol{X}, m)\cos[i\omega L_t - \varphi_i(\boldsymbol{X}, m)] \quad (1)$$

where D is the diurnal anomaly at the geolocation $\boldsymbol{X}$, month m, and local time L_t in a day, D_i and φ_i (i = 1 and 2) represent the amplitude and phase of the diurnal and semi-diurnal components which are functions of month and geolocation; t indicates year and $\omega = 2\pi/24$, the frequency of diurnal cycle. Equation 1 is a physically based diurnal model during daytime. However, it becomes an empirical model for the nighttime thermal decay. As such, it is referred to as a semi-empirical or semi-physical diurnal model in this study. Chen et al. (2018) used this model for diurnal drift adjustment for all the AMSU-A channels. Note that L_t varies from year to year, but we only solve for monthly climatology for the diurnal amplitude D_i and the phase φ_i and ignore their annual variations. As such, yearly changes in the diurnal anomaly D are caused only by the annual variations in L_t. This assumption does not appear to cause biases in the diurnal adjustment as shown in the following.

Second, in Po-Chedley et al. (2015), diurnal adjustment was applied only to the tropical area (20°S–20°N). Here we apply Equation 1 globally to zonal mean latitudinal belts for each month over ocean and land with different fitting coefficients. This allows the adjustment to account for different temporal patterns of diurnal drifts at different geolocations. With these extensions, and expanding Equation 1 into summation of sine and cosine terms using Ptolemy's identity, the diurnal anomaly is written as

$$D_j(\boldsymbol{X}, m, L_j) = a_j(\boldsymbol{X}) + \sum_{i=1}^{2}\left[b_i(\boldsymbol{X}, m)\sin(i\omega L_j) + c_i(\boldsymbol{X}, m)\cos(i\omega L_j)\right], \quad (2)$$

where the subscript j represents a satellite to be adjusted, ascending and descending nodes separately; L_j is the ascending or descending local overpass time of satellite j at year t and month m, and $b_i(\boldsymbol{X},m)$ and $c_i(\boldsymbol{X},m)$ are periodic functions characterizing the amplitudes of the monthly diurnal and semi-diurnal components with a period of 1 year (i.e., both $b_i(\boldsymbol{X},m)$ and $c_i(\boldsymbol{X},m)$, $i = 1, 2$, contain 12 coefficients representing 12 months at geolocation $\boldsymbol{X}$). Here the coefficients $b_i(\boldsymbol{X},m)$ and $c_i(\boldsymbol{X},m)$ are assumed the same for different satellites but different for ascending and descending nodes and different instrument types (MSU and ANSU-A). The coefficient $a_j(\boldsymbol{X})$ is a combination of fitting coefficient and the yearly mean difference between satellite j and the reference satellite.

With Equation 2, the adjustment to satellite j due to diurnal sampling drift can be written as,

$$TB'_j(\boldsymbol{X}, t, m) = TB_j(\boldsymbol{X}, t, m, L_j) - D_j(\boldsymbol{X}, m, L_j) \quad (3)$$

where $TB_j(\boldsymbol{X}, t, m, L_j)$ represents the monthly brightness temperature (ascending or descending) for satellite j at the local overpass time L_j and $TB'_j(\boldsymbol{X}, t, m)$ the adjusted brightness temperature for satellite j. For overlapping satellite pairs, Equation 3 can be expressed as

$$TB'_j(\boldsymbol{X}, t, m) - TB'_k(\boldsymbol{X}, t, m) = TB_j(\boldsymbol{X}, t, m, L_j) - TB_k(\boldsymbol{X}, t, m, L_k) - D_j(\boldsymbol{X}, m, L_j) + D_k(\boldsymbol{X}, m, L_k) \quad (4)$$

By minimizing inter-satellite differences between satellite pairs ($\Delta TB'_{jk} = TB'_j - TB'_k$, the left-hand side of Equation 4), the coefficients a, b, and c in Equation 2 can be solved through multiple linear regression for both satellites and for each iterative geolocation $\boldsymbol{X}$. Note that the coefficients $b(\boldsymbol{X},m)$ and $c(\boldsymbol{X},m)$ for all 12 months and the annual mean coefficient $a_j(\boldsymbol{X})$ are solved simultaneously in a single multiple regression process.

We assume a common diurnal adjustment for the three AMSU-A satellites, NOAA-15, NOAA-18, and NOAA-19, meaning the coefficients b_i and c_i ($i = 1, 2$) in Equation 2 are the same for the three satellites. These common monthly fitting coefficients are solved simultaneously using multiple linear regressions. RTMT is used as a common reference (the diurnal anomaly equals zero for RTMT) for the three satellites which provides a strong constraint on the solutions. Since RTMT was defined as an average from the MetOp-A ascending and descending orbits, the adjusted brightness temperature was also defined as means of ascending and descending orbits. Similarly, a common diurnal adjustment is assumed for all the MSU satellites (b_i and c_i are the same for all the MSU satellites). In MSU regressions, all overlaps from TIROS-N through NOAA-14 were used at the same time and the diurnal adjusted NOAA-15 in the earlier step was used as a reference (anchor). This allows the MSU diurnal adjustment for TIROS-N through NOAA-14 to be linked to RTMT through the overlaps between NOAA-14 and NOAA-15. We do not intend to resolve the complete 24-hr diurnal cycles with the regression. This is because the model parameter numbers in Equation 2 (b_i and c_i, $i = 1, 2$, and L_j) are insufficient to characterize the full diurnal cycles in both daytime and nighttime, which involve different physical processes. The empirical model for the nighttime diurnal cycle (diurnal plus semi-diurnal components) only approximates the thermal decay process. Although its formula is the same as the daytime physical model, different sets of model parameters are expected to represent the two different diurnal segments. Furthermore, the transition period near sunrise features a peculiar, non-smooth diurnal pattern where temperature rises rapidly from the end of nighttime attenuation to the start of daytime quasi-sinusoidal diurnal patterns (Figure 6). This period coincides with the orbital drifting range of the MSU and AMSU-A morning satellites as well as afternoon satellites whose orbits drifted to the transition period (e.g., NOAA-14). Model parameters that best fit the transition period would have the best effect in bias removals for these satellites. With these considerations, we resolve the ascending and descending orbits separately in regressions for both the MSU and AMSU-A satellites. This allows five parameters (b_i and c_i, $i = 1, 2$, and L_j) to model each of the ascending and descending diurnal segments. Also, land and ocean are solved separately because of their large differences in amplitudes in diurnal cycles. Only the diurnal component is included in resolving diurnal cycles over ocean since their magnitudes there are small.

Figure 7 shows yearly mean global and tropical (20°S–20°N) diurnal cycles for the AMSU-A and MSU satellites over land and ocean, respectively, and their comparisons to model-simulated diurnal cycles. The model simulations were taken from the RSS group, which were based on hourly output from a 5-year run of the National Center for Atmospheric Research's (NCAR) Community Climate Model (CCM3; Kiehl et al., 1996). This

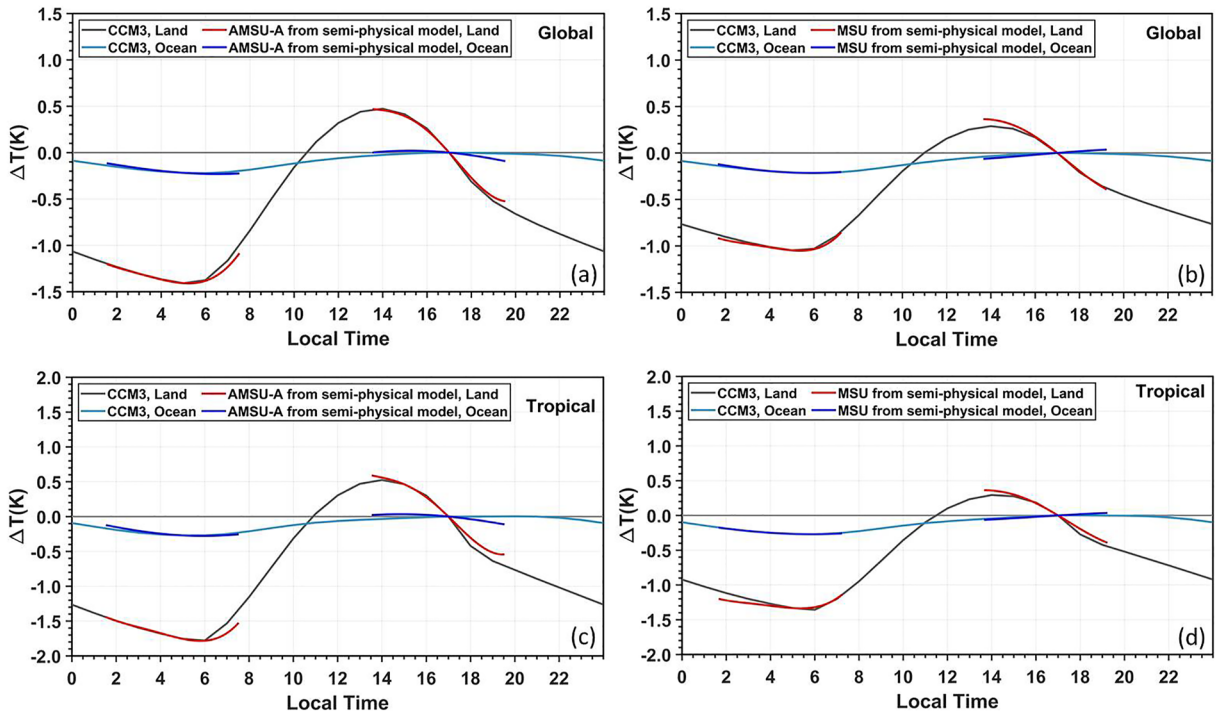

Figure 7. Yearly mean diurnal anomalies obtained from the semi-physical model and their comparisons to the CCM3 climate model simulations. (a) AMSU-A over the global land and ocean; (b) MSU over the global land and ocean; (c) AMSU-A over the topical (20°S–20°N) land and ocean; (d) MSU over the topical land and ocean. The left and right branches in the semi-physical model solutions are for descending and ascending orbits, respectively. The reference times for the diurnal anomalies are the means of the LECTs, which are 17:00 p.m. for ascending and 5:00 a.m. for descending orbits for both the AMSU-A and MSU satellites (Figure 1). These reference times in the semi-physical model solutions are forced to match the CCM3 simulations at the same times to aid in comparisons between the two types of the diurnal cycles.

model-simulated diurnal cycle was used for diurnal adjustments in earlier versions of RSS (Mears et al., 2003) and STAR (Zou & Wang, 2011) TMT data sets. Figure S1 in Supporting Information S1 shows similar comparisons except for monthly diurnal anomalies averaged over selected regions. As seen, diurnal cycles from the semi-physical model generally agree well with the CCM3 simulations. But the MSU diurnal anomalies from the semi-physical model exhibited slightly different amplitudes near 2 p.m. In addition, differences between the semi-physical diurnal model and CCM3 simulations occurred during the transition periods over land: the morning transition from the nighttime attenuation to the daytime quasi-sinusoidal patterns and their reversed transition in the afternoon. These differences were more obvious in the monthly diurnal cycles over selected regions (Figures S1 in Supporting Information S1). It is hard to determine from their appearances which one would more closely represent the real diurnal patterns during these periods. On one hand, the semi-physical model is only an approximation of diurnal changes during the transition periods. On the other hand, it is also challenging for climate models to correctly simulate the transition periods due to complex boundary layer processes involved and, therefore, biases may exist in these simulations (Angevine et al., 2020). Fortunately, the semi-physical diurnal model performs quite well in removing inter-satellite difference trends (Figures 9 and 10). This provides justification for using it for diurnal drift adjustment.

Figure 8 shows inter-satellite difference time series ($\Delta TB_{jk} = TB_j - TB_k$) compared with diurnal cycle differences ($\Delta D_{jk} = D_j - D_k$) obtained from the semi-physical model for all satellite pairs from TIROS-N to RTMT, land and ocean and ascending and descending orbits separately. Figures S2–S6 in Supporting Information S1 show similar plots but averaged over different regions. As seen, the derived diurnal cycle differences from the semi-physical model agree very well with the observed inter-satellite differences in both the seasonal variability and long-term trends for the AMSU-A satellite pairs over ocean (Figure 8a) and for all MSU and AMSU-A satellite pairs over land (Figure 8b). However, the seasonal variability in the observed difference time series are larger than the semi-physical model solutions for most MSU satellite pairs over ocean (Figure 8a). This occurred because the observed differences between these satellite pairs contained signals of warm target temperature variability that

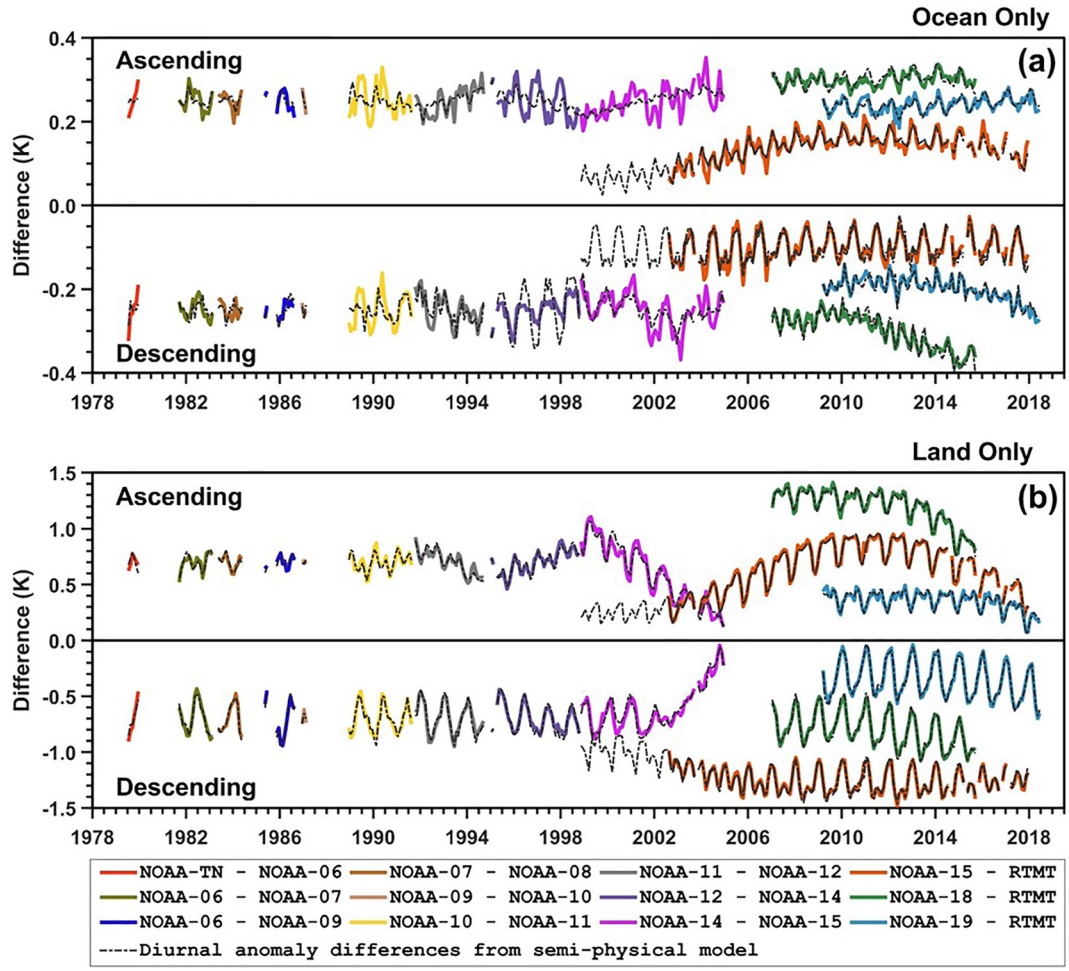

Figure 8. Inter-satellite differences ($\Delta TB_{jk} = TB_j - TB_k$, colored solid lines) and diurnal anomaly differences ($\Delta D_{jk} = D_j - D_k$, dashed lines) derived from the semi-physical model for (a) over the global ocean and (b) over the global land. Differences were grouped into ascending and descending data separately by adding constant offsets to different satellite pairs for an adjustment. As such, the vertical temperature coordinate does not necessarily represent the actual values or signs of the mean diurnal anomaly differences, but they represent the magnitudes of the seasonal cycle and drifting range of the diurnal anomaly differences. The NOAA-15 diurnal anomalies during the 3.5-year period from November 1998 to July 2002 were predicted from the semi-physical model based on regression coefficients obtained from its overlaps with RTMT during August 2002–December 2017.

cannot be completely represented by diurnal drifting processes. This misfit in seasonal variability will be further removed by adjusting the warm target temperature effect as described in the next section.

Figures 9a and 9b show inter-satellite difference time series after the diurnal adjustment ($\Delta T B'_{jk} = T B'_j - T B'_k$, or difference between ΔTB_{jk} and ΔD_{jk}, see Equation 4) for the averages of ascending and descending orbits for all satellite pairs over ocean and land, respectively. Figure 10 further shows statistics of the standard deviations and trends for the $\Delta T B'_{jk}$ time series for all satellite pairs. The means of the $\Delta T B'_{jk}$ time series are zero at three decimal places for all satellite pairs (Figures 9a and 9b). The standard deviations are from 0.01 to 0.03 K over ocean and from 0.02 to 0.05 K over land, respectively (Figures 10a and 10b). The trends of inter-satellite difference time series are smaller than 0.05 K/decade for most satellite pairs with longer overlaps and for both land and ocean, with a maximum trend of −0.41 K/decade for the satellite pair between NOAA-6 and NOAA-9 over land. These standard deviations and difference trends are to be further reduced by adjustment of the warm target effect, particularly over the ocean.

As mentioned earlier, diurnal drift and calibration drift are generally mixed together for satellites with orbital drifts. As such, recalibration performance for these satellites shall be analyzed together with diurnal drift

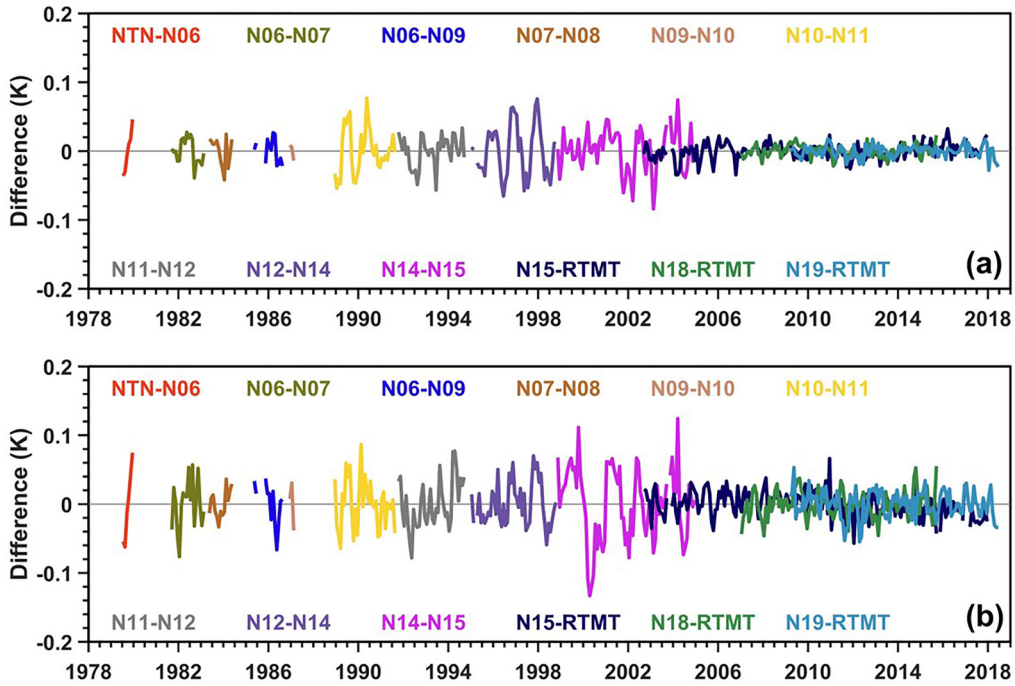

Figure 9. Inter-satellite difference time series for satellite pairs between those from TIROS-N to RTMT after diurnal drift adjustments for (a) over the global ocean and (b) over the global land, respectively.

adjustment. With diurnal adjustment completed, here we continue the discussion of recalibration performance in Section 3 for NOAA-15 during its overlaps with Aqua and NOAA-14 and for NOAA-18 during its entire observation period. As seen, the dark blue curves in Figures 5a and 5b show the difference time series between the recalibrated NOAA-15 and RTMT over the global ocean and land, respectively. Obvious drifts between them were seen during 2002–2007. These drifts actually represented those between the recalibrated NOAA-15

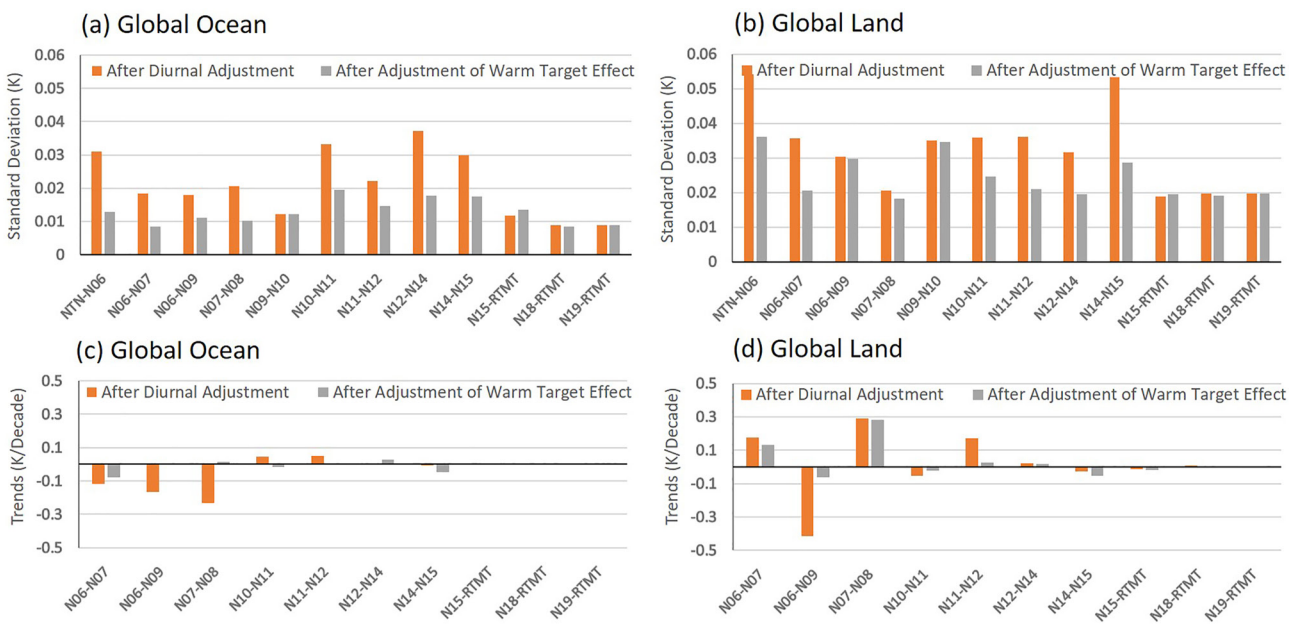

Figure 10. Statistics of inter-satellite difference time series between satellite pairs after adjustment of diurnal drift (purple) and warm target effect (gray). (a) Standard deviations over ocean; (b) Standard deviations over land; (c) Difference trends over ocean; (d) Difference trends over land. Note that the difference trends for the satellite pairs between TIROS-N and NOAA-6 and between NOAA-9 and NOAA-10 were not shown since their overlaps were too short to have a meaningful trend.

and non-recalibrated Aqua since the latter was the only satellite included in RTMT during this period (Zou et al., 2021). During this period, the NOAA-15 orbit monotonically drifted for about 2.5 hr from 7:30–5 p.m. in ascending node (7:30–5 a.m. in descending node, Figure 1). This orbital drift coincided with the transition period near sunrise in diurnal cycles where temperature rises rapidly (Figure 6). This caused a noticeable diurnal effect on NOAA-15 which affected the analysis of its recalibration performance. After diurnal adjustment, the difference trends between NOAA-15 and RTMT are near-zero for their entire overlaps from 2002 to 2017 over both land and ocean (Figures 9 and 10). This implies that removal of the cooling drift in NOAA-15 in the recalibration step in Section 3 reduced not only its trend differences relative to MetOp-A but also its trend differences relative to Aqua. Similarly, difference trends between the recalibrated NOAA-14 and NOAA-15 were close to zero during their overlaps from 1998 to 2004 after diurnal drift adjustments over both land and ocean (Figures 9 and 10). In contrast, large trend differences between these two satellites still remained during their overlaps even after diurnal adjustment if calibration drifts were not removed (Mears & Wentz, 2016). This implies that recalibration for both NOAA-14 and NOAA-15 has most likely removed their calibration drifts correctly. Finally, the recalibrated NOAA-18 still exhibited an obvious cooling drift of about 0.08 K/decade relative to MetOp-A during 2008–2016 over the global ocean (Figure 2b). This drift was caused by its nearly 4-hr monotonically orbital drift during the same period (Figure 1) that cannot be removed by recalibration. After diurnal drift adjustment, the difference trends between NOAA-18 and RTMT were reduced to near-zero over both land and ocean during the entire NOAA-18 observations (Figures 9 and 10). This implies that recalibration in Section 3 had correctly removed calibration drifts in NOAA-18 observations. Overall, the simultaneous removal of inter-satellite trend differences for multiple satellite pairs with common diurnal models for the MSU and AMSU-A satellites strongly suggest that removal of calibration drifts in the recalibration step and diurnal drift removal in diurnal adjustments are consistent with each other. In order words, it is most likely that each of the recalibration and diurnal adjusting processes has removed the right amount of bias drift of its own sources.

6. Adjustment of Warm Target Effect and Data Merging

A blackbody warm target was used to calibrate the MSU and AMSU-A raw counts observations to obtain level-1c radiances (Appendix A). The warm target temperature was measured by the Platinum Resistance Thermometers (PRTs) embedded on the blackbody. There were 5 PRTs for AMSU-A channel 5 and 2 PRTs for MSU channel 2, respectively. An average of available good measurements from these PRTs were used to represent the warm target temperature. The blackbody target temperature exhibited large seasonal variability and long-term trends for most MSU satellites and NOAA-15 due to solar heating induced by changes in the angle of incident solar radiation on the satellite (Zou & Wang, 2011). These variability and trends were largely reduced by the level-1c recalibration with the SNO approach (Appendix A). However, small residual variability and biases still exist due to imperfect calibration. These residual biases need to be removed before satellite merging. Christy et al. (2000) developed an empirical algorithm to remove the radiance errors due to this warm target effect which was implemented in all the existing STAR, UAH, RSS, and UW data sets. This approach finds a best fitting empirical relationship between the correction term of the level-3 gridded brightness temperatures and warm target temperatures and then removes the best fit from the unadjusted time series. Using TB_a and TB_u to respectively represent adjusted and unadjusted brightness temperatures, this empirical approach can be mathematically expressed as

$$TB_a = TB_u - \beta - \alpha T'_w \tag{5}$$

where T'_w denotes the warm target temperature anomaly, β a constant and α the warm target factor (Christy et al., 2000; Mears et al., 2003). Applying Equation 5 to overlapping satellite pairs, we obtain

$$TB_{ai} - TB_{aj} = TB_{ui} - TB_{uj} - \beta_i + \beta_j - \alpha_i T'_{wi} + \alpha_j T'_{wj} \tag{6}$$

where the subscripts i and j represent satellite indexes in overlapping satellite pairs which go through all satellites from TRIOS-N to NOAA-18. This forms a set of multiple regression equations to solve for the coefficients β and α by minimizing the left-hand side of Equation 6 for all satellite pairs. Only the global ocean mean data were used for TB_u and T'_w in this regression and NOAA-19 was excluded since its warm target effect was negligible (Appendix A).

Table 2 lists the resulting warm target factors solved from regressions for all satellites. The values of the target factors here are one order of magnitude smaller than those in RSS and UAH data sets for most satellites (Mears &

Table 2
Warm Target Factors (10^{-2})

NTN	N06	N07	N08	N09	N10	N11	N12	N14	N15	N18
1.55	−0.27	0.53	1.50	−0.47	−0.58	0.23	−0.45	0.77	0.15	−0.29

Wentz, 2009; Spencer et al., 2017). This is because RSS and UAH used operational calibrated level-1c radiances, which contained larger warm target contamination, to generate their TMT data sets. In contrast, our recalibration in Appendix A had already largely reduced the warm target effect.

Figure 10 shows statistics of standard deviations and trends of inter-satellite difference time series between different satellite pairs after adjustment of the warm target effect. These statistics are compared to those before the adjustment (after diurnal drift adjustment). As seen, the adjustment largely reduced the standard deviations for most satellite pairs from TIROS-N to NOAA-15 over both land and ocean. The adjustment also largely reduced the difference trends for most satellite pairs over the ocean, resulting in their values less than 0.08 K/decade for all satellite pairs after the adjustment. The adjustment also largely reduced the difference trends to less than 0.05 K/decade for most satellite pairs with relatively longer overlaps over land, but the difference trends between NOAA-7 and NOAA-8 was still larger after the adjustment (up to 0.28 K/decade). This is not a concern since NOAA-8 had only 1 year of observations which fully overlapped with NOAA-7 (Table 1 and Figure 1). Their larger trend differences over short periods had negligible effect on trends of other satellite pairs or longer periods of the time series.

Figure 11 shows statistics of standard deviations and absolute values of difference trends averaged over all satellite pairs. In addition to adjustments of diurnal drift and warm target effects, the statistics also include those after SNO recalibration and frequency adjustment. In general, both the standard deviations and absolute values of difference trends were large over land after the SNO recalibration but they were significantly reduced by the diurnal drift adjustment. The reduction for the standard deviation was from 0.079 to 0.032 K and trends from 0.22 K/decade to 0.12 K/decade, respectively. The adjustment of warm target effect further reduced the standard deviations and the averaged difference trends. Over the ocean, both standard deviations (0.024 K) and difference trends (0.065 K/decade) were already small after the SNO recalibration. The adjustments of diurnal drift and warm target effects further reduced the standard deviations and difference trends to 0.013 K and 0.019 K/decade, respectively.

Figure 12 shows monthly global mean inter-satellite difference time series for all satellite pairs after adjustment of the warm target effect. As seen, inter-satellite differences for each satellite pair were zero, the standard deviations of inter-satellite differences were minimized, and trend differences between satellite pairs were close to zero. As a last step, these recalibrated and adjusted MSU, AMSU-A and RTMT data were simply averaged on each grid cell to generate a merged TMT time series from November 1978 to June 2021. This newly merged time series is named STAR Version 5.0 (V5.0) TMT data set.

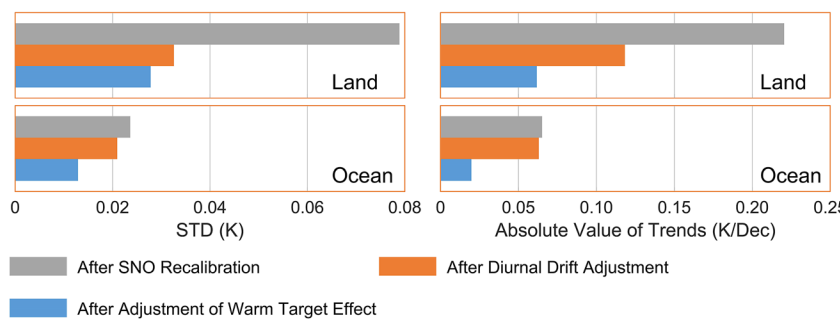

Figure 11. Averages of standard deviations (STD, left) and absolute values of difference trends (right) over satellite pairs from TIROS-N to RTMT after each of the following sequential adjustment steps: SNO recalibration, diurnal drift adjustment, and adjustment of warm target effect. Difference trends for the satellite pairs between TIROS-N and NOAA-6 and between NOAA-9 and NOAA-10 were not included in the calculations of trend averages since their overlaps were too short to have a meaningful trend.

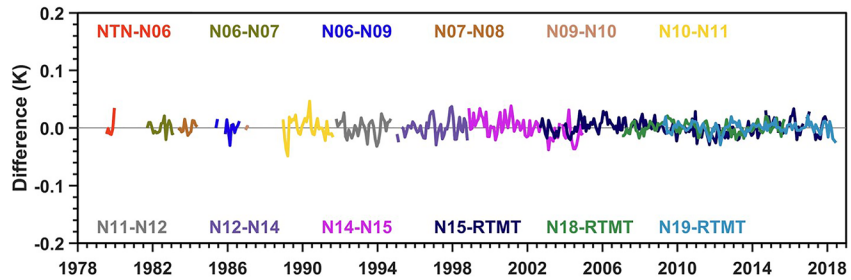

Figure 12. Global monthly mean inter-satellite difference time series after adjustment of warm target effect.

7. Comparisons With Existing Data Sets

Figure 13 shows anomaly time series of STAR V5.0 along with STAR V4.1, RSS V4.0, and UAH V6.0 over ocean, land, and globe, respectively, for a comparison. We show monthly anomaly time series but with yearly mean differences between different data sets to focus on discussions of trend differences. As seen, different versions of the anomaly time series show excellent agreement in variability (Figures 13a, 13c, and 13e). This is expected since all of these data sets used channels with the same frequency that have the same sensitivity to TMT changes. But total trends are quite different among different data sets. The STAR V5.0 produced a global-mean trend of 0.092 ± 0.043 K/decade during the entire observation period from January 1979 to June 2021. However, the STAR V4.1 produced a global-mean trend of 0.156 ± 0.052 K/decade, 0.064 K/decade (71%) higher than the STAR V5.0 trend during the same period. The global-mean trend of RSS data was 0.139 ± 0.049 K/decade, 0.046 K/decade (51%) higher than STAR V5.0 during the same period. The higher warming trends in STAR V4.1 and RSS V4.0 are also seen in their separate ocean and land means compared to STAR V5.0. In contrast, the UAH V6.0 trends are close to STAR V5.0 within 10% over ocean, land and globe (Figures 13b, 13d, and 13f).

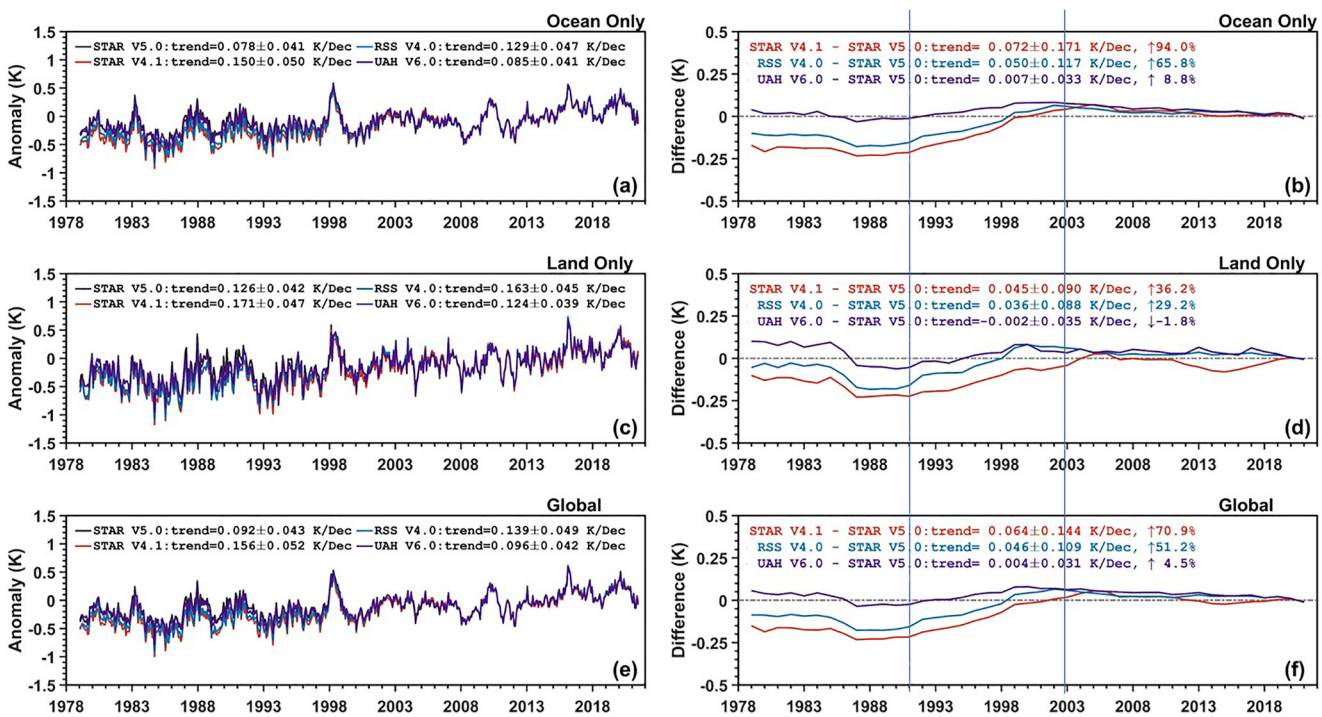

Figure 13. Comparisons of TMT time series between existing data sets and STAR V5.0 from the present study during January 1979–June 2021. (a) TMT monthly anomalies averaged over the global ocean; (b) Annual-mean anomaly difference time series between existing data sets and STAR V5.0 over the global ocean; (c) TMT monthly anomalies averaged over the global land; (d) Annual-mean anomaly difference time series between existing data sets and STAR V5.0 over the global land; (e) Global-mean TMT monthly anomalies; (f) Global annual mean anomaly difference time series between existing data sets and STAR V5.0. Time series are plotted so that their mean differences during January 2020–June 2021 are zero. Vertical lines on the right panels represent the end of NOAA-10 near 1991 and start of RTMT on August 2002, respectively. Only statistical uncertainties were included to represent trend uncertainties in these plots (see Table 4 and related discussions)

The difference time series between different data sets (Figures 13b, 13d, and 13f) provided clues on how their trend differences occurred. We divide the entire observations into three subperiods and analyze them separately: 1979–1991 for TIROS-N to NOAA-10, 1991–2002 for NOAA-11 to NOAA-14, and 2002–2021 for RTMT (Aqua to NOAA-20). During the period of 2002–2021, all existing data sets show downward trends relative to STAR V5.0 over the ocean (Figure 13b). Since diurnal effects are small over ocean, these downward trends in the existing data sets relative to STAR V5.0 are attributed to a common cause−NOAA-15 used in those data sets. NOAA-15 had a cooling drifting error before recalibration (Figure 2a), which was removed in our recalibration in this study. The STAR V5.0 used the recalibrated NOAA-15 data which was consistent with and had no drifting errors relative to RTMT. On the other hand, all the other data sets used the NOAA-15 data of before recalibration, although different data sets used different cutoff dates in the NOAA-15 observations. As such, the cooling drifting errors in NOAA-15 before recalibration had caused the existing data sets to have a downward cooling drift relative to STAR V5.0.

In the second subperiod from 1991 to 2002, the STAR V.4.1 and RSS 4.0 exhibited a similar large upward trend relative to STAR V5.0 over the ocean. This occurred because the former data sets used the *TB* data of before recalibration for NOAA-11 to NOAA-14 which had large spurious warming drifts up to 0.19 K/decade (Figure 3b). On the other hand, the STAR 5.0 used the recalibrated *TB* data in which the recalibrated NOAA-15 was used as a reference and NOAA-11 through NOAA-14 were sequentially adjusted to it. This had a cascading effect that trends on NOAA-11 through NOAA-14 were lowered substantially via approximately linear trend removal (Figure 3b). This cascading removal of the large spurious warming drifts in NOAA-11 through NOAA-14 had caused much lower warming trends in STAR V5.0 relative to STAR V4.1 and RSS V4.0 during 1991–2002 and the entire observation period from 1979 to 2021 (Figure 13b).

The UAH V6.0 also had a warming trend relative to STAR V5.0 during 1991–2002 over the ocean, but the magnitude was much smaller than those in STAR V4.1 and RSS V4.0 (Figure 13b). Note that UAH V6.0 had applied a trend adjustment for NOAA-14 relative to NOAA-15 and NOAA-12 and for NOAA-11 relative to NOAA-10 and NOAA-12 (Spencer et al., 2017). These adjustments appeared to have reduced the spurious warming effects in NOAA-14 and NOAA-11 and produced a trend more consistent with STAR V5.0 during 1991–2002 and the entire observation period from 1979 to 2021.

In the third subperiod from 1979 to 1991, trend differences between STAR V5.0 and the other existing data sets were small over ocean. This occurred most likely because calibration drift in NOAA-10 was relatively small (Figure 3b) and that no additional calibration was conducted for NOAA-9 to TIROS-N in this study (Appendix A). As a result, calibration drifts, if existing, would be similar between different data versions for satellites from NOAA-10 to TIROS-N. This resulted in consistent TMT trends during this period for different data sets.

Over land, the RSS and UAH data drifted cooler relative to STAR V5.0 during the 2002–2021 period, but the STAR V4.1 time series wiggles relative to STAR V5.0 during the same period (Figure 13d). During the 1991–2002 subperiod, the RSS V4.0, STAR V4.1 and UAH V6.0 data sets still drifted warmer relative to STAR V5.0, but the magnitudes were smaller than those over the ocean. During the 1979–1991 subperiod, all the existing data sets exhibited flat trends relative to STAR V5.0 in most times except an obvious downward trend during 1985–1987. These behaviors in trend differences over land were different from over the ocean and thus suggested impact of the diurnal drift adjustment over land. The total trends over land in the STAR V4.1 and RSS V4.0 during the entire observation periods from 1979 to 2021 were warmer than STAR V5.0 by 0.045 K/decade (36%) and 0.036 K/decade (29%), respectively. In contrast, the UAH V6.0 warming trends were close to STAR V5.0 within 0.002 K/decade (1.8%) over land for the entire observation period.

In summarizing the above comparisons, Table 3 lists various adjustments for different types of biases involved in different data sets. In most cases, different data sets used different approaches to adjust the same type of biases. Of the various adjustments, the primary reason causing the larger global trend differences in STAR V5.0 from the exiting data sets, particularly STAR V4.1 and RSS V4.0, is the recalibration removal of the NOAA-15 spurious cooling drift and spurious warming drifts in NOAA-11, NOAA-12, and NOAA-14. Differences in diurnal drift adjustments are of secondary importance to their trend differences.

8. Trends and Uncertainties in STAR V5.0 TMT Time Series

The estimated uncertainty in trend detection in the RTMT time series is 0.012 K/decade (Zou et al., 2021). It is desirable to estimate trend uncertainty in STAR V5.0 for the entire observation period from 1979 to present.

Table 3
Adjustments for Different Types of Biases Involved in Different Data Sets

Type of biases	STAR V5.0 (this study)	STAR V4.1 (Zou et al., 2015)	RSS V4.0 (Mears & Wentz, 2016)	UAH V6.0 (Spencer et al., 2017)
NOAA-15 spurious cooling drift	Removed by recalibration	No adjustment but with data cuts	No adjustment but with data cuts	No adjustment but with data cuts
Spurious warming drift in NOAA-11, NOAA-12, and NOAA-14	Removed by recalibration	No adjustment	No adjustment	Adjusted NOAA-11 and NOAA-14 relative to their neighboring satellites
Diurnal sampling drift	Adjustment with observation-based semi-physical model	Adjustment with observation-based empirical function	Climate model simulation plus observational adjustment	Adjustment with observation-based empirical approach
Channel Frequency differences	CRTM simulation plus observational adjustment	CRTM simulation plus observational adjustment	Empirical adjustment based on MSU and AMSU-A overlapping observations	Adjusted by matching MSU and AMSU-A weighting functions with different viewing angles
Warm target effect	Recalibration removal plus empirical fitting function adjustment	Recalibration removal plus empirical fitting function adjustment	Adjustment with empirical fitting function	Adjustment with empirical fitting function

The TMT trend uncertainties are divided into *structure uncertainty* and *internal uncertainty* (Mears et al., 2011). Drifting errors from instrument calibration are systematic errors and thus a source of structure uncertainty in trend detection. Structure uncertainty can be large sometimes which could be estimated by comparing observations from different instrument types or the same data products but developed by different research groups. The large trend differences between STAR V5.0 and STAR V4.1 (and also RSS V4.0) as analyzed in Section 7 were mainly caused by recalibration removal of the spurious warming trends in NOAA-11 through NOAA-14 and thus are part of the structure uncertainty in the TMT trend estimates. Sources of error causing internal trend uncertainty may include those from observational sampling, adjustments of diurnal drift and warm target effects, and adjustments of channel frequency differences between MSU and AMSU-A. In a Monte Carlo simulation, Mears et al. (2011) obtained a relatively small 2σ internal uncertainty of 0.012 K/decade for near-global TMT time series when all the error sources mentioned above were considered, excluding diurnal drift adjustment. Also using statistical simulations, Po-Chedley et al. (2015) obtained 2σ internal trend uncertainties of 0.035 K/decade and 0.020 K/decade over the tropical land and ocean, respectively, for the error sources from adjustments of diurnal drift and warm target effects.

Here we focus on uncertainty estimates from the diurnal drift adjustment since global TMT trends are sensitive to errors in diurnal adjusting algorithms (Mears & Wentz, 2016). Error estimates from the adjustment are critical for statistical simulations. For simplicity and easy comparisons, we followed Mears et al. (2011) study in which a ±50% of error, independent of geolocation, was assumed for the diurnal adjustment. This assumed error is proportional to the magnitudes of diurnal adjustment with larger errors for larger adjustments. Using this error estimate, we generated 2,500 random errors and then added them to the optimal diurnal adjustment from the semi-physical model. The time series was then remerged following steps as described in Sections 5 and 6 for each of the perturbated diurnal adjustment, and trends from the merged time series with adjustment errors in it

Table 4
TMT Trends and Uncertainties (2σ or 95% Confidence Interval) for Three Periods of Interest

	01/1979–06/2021						01/1979–12/1996					08/2002–06/2021				
Time period	Trend	IU_T	IU_R	IU_D	IU_P	SU	Trend	IU_R	IU_D	IU_P	SU	Trend	IU_R	IU_D	IU_P	SU
Ocean mean	0.078	0.014	0.004	0.003	0.006	0.041	0.027	0.008	0.020	0.006	0.097	0.187	0.001	0.001	0.019	0.135
Land mean	0.126	0.040	0.006	0.037	0.009	0.042	0.087	0.012	0.041	0.014	0.137	0.186	0.001	0.008	0.020	0.100
Global mean	0.092	0.019	0.004	0.013	0.007	0.043	0.044	0.007	0.026	0.009	0.112	0.187	0.001	0.003	0.020	0.126

Note. The abbreviations IU_R, IU_D, and IU_P stand for internal uncertainties from recalibration, diurnal drift adjustment, and error propagation, respectively, and SU for statistical uncertainty. IU_T stands for total internal uncertainty which is the square root of summations over the squared IU_R, IU_D, IU_P, and the internal uncertainty of 0.012 K/decade from all other adjustments obtained by Mears et al. (2011). The SU was calculated with autocorrelation adjustment. Units are in K/decade.

were calculated for periods of interest. Table 4 lists the mean trends and their 2σ uncertainties (95% confidence intervals) from these statistical simulations for three periods of interest: the entire observation period from 1979 to 2021, the first half period from 1979 to 1996, and the second half period from 2002 to 2021. The large warming spike in the 1998 El Nino event (e.g., Figure 13e) was intentionally excluded in the first and second half periods to avoid end-point effects in trend calculations. The mean trend values in the three periods in Table 4 are exactly the same as those calculated from the STAR V5.0 time series. Trend uncertainties in the first half period were 0.02 K/decade and 0.04 K/decade for the ocean and land means, respectively. These values are quite close to those in Po-Chedley et al. (2015) for trend uncertainties in the tropical TMT time series. Uncertainties in the second half period are smaller than 0.008 K/decade for land and 0.003 K/decade for the ocean and global means. These small uncertainties are expected since RTMT during this period served as a strong constraint for diurnal adjustment that suppressed uncertainties. The small uncertainty in the second half period resulted in overall smaller uncertainties for the entire observation period from 1979 to 2021, especially for the ocean and global means.

We also estimate internal uncertainties from the recalibration process. Recalibration using SNO matchups in Appendix A incurred model uncertainty (linear vs. nonlinear assumptions on instrument degradations over time) as well as observation uncertainty. The observation uncertainty, being referred to as prediction intervals in regressions (Svetunkov, 2022), gives a larger error estimate than model uncertainty and thus provides an upper limit in recalibration uncertainties. The observation uncertainty in SNO regressions is represented by the mismatch errors plus statistical noise in SNO samplings (Zou et al., 2006). The mismatch errors are ignored here and the statistical noise in SNOs equals to the instrument noise equivalent differential temperature (NEDT) multiplied by $\sqrt{2}$ (Zou et al., 2006). This gives an uncertainty estimate about 0.35 K (NEDT ~0.25 K for AMSU-A channel 5, Mo, 1996) in recalibration. This error estimate was then used to generate random perturbations to each of the satellites from NOAA-10 through NOAA-19 at each month and each grid point independently to estimate trend uncertainties similar to statistical simulations in the diurnal drift adjustment. Table 4 lists the 2σ trend uncertainties from 2,500 statistical simulations for the three periods of interest as analyzed in the diurnal drift adjustment. In general, trend uncertainties from recalibration behaved similarly to those from the diurnal drift adjustment for all the three periods of interest except their magnitudes are smaller. This is expected since the error estimate from recalibration (0.35 K) is smaller than the diurnal drift adjustment (±50% of the diurnal drift adjustment), especially over land.

In addition to the above-mentioned error sources, STAR V5.0 has another source of uncertainty—propagation of uncertainty from RTMT to the earlier satellites through adjustments of diurnal drift and warm target effects in the backward merging process. We also use statistical simulations, up to 2,500 times, to estimate this uncertainty. In each simulation, a randomly sampled trend, representing bias drifting errors, with a standard deviation (1σ) of 0.012 K/decade, was added to all grid points in all months in RTMT. This perturbated RTMT is then used as a reference to generate a new merged time series from 1979 to 2021 using the optimal adjusting algorithms for diurnal drifts and warm target effects. The 2σ trend uncertainties of the remerged time series from these simulations are also listed in Table 4 for the three periods of interest. The internal uncertainty in the second half period is 0.020 K/decade for all ocean, land, and global means, slightly smaller than the given 2σ uncertainty of 0.024 K/decade in RTMT during the same period. This is expected since more satellite observations (NOAA-15, NOAA-18, and NOAA-19) were included in STAR V5.0 which would reduce the uncertainties inherited in RTMT during the same period. Uncertainties in the first half and the whole periods (e.g., 0.007 K/decade for global means during the entire period) are much smaller than the given 2σ uncertainty in RTMT, suggesting that the merging process had reduced the uncertainty initially imposed on RTMT. The reduction, rather than amplification, of uncertainty in error propagations by the merging procedure is an excellent feature that results in controlled uncertainties in the longer time series. On another note, uncertainties due to diurnal drift adjustment were largest in the first half period. This is in contrast to uncertainties due to error propagation which were largest in the second half period.

Total internal uncertainty for the entire observation period from 1979 to 2021 was calculated as the square root of summations over the squared uncertainties from recalibration, diurnal drift adjustment, error propagation, and the internal uncertainty of 0.012 K/decade from all other sources (Mears et al., 2011). This gives a total internal uncertainty of 0.019 K/decade over the globe, only one-half of the total internal uncertainty of 0.042 K/decade obtained in Mears et al. (2011) study. Possible reason for this is that the large inter-satellite trends between NOAA-14 and NOAA-15 before recalibration (Figure 3a) were treated as a source of internal uncertainty in Mears et al. (2011). In our study, however, relative trend between NOAA-14 and NOAA-15 was removed by recalibration and its related uncertainties were reflected in the TMT structure uncertainty. Of interest, the total

Table 5
Total Tropospheric Temperature (TTT) Trends From STAR V5.0 and Their Uncertainties for Three Periods of Interest

Time period	01/1979–06/2021	01/1979–12/1996	08/2002–06/2021
Ocean mean	0.126 ± 0.043	0.098 ± 0.099	0.214 ± 0.136
Land mean	0.183 ± 0.058	0.187 ± 0.144	0.234 ± 0.102
Global mean	0.142 ± 0.047	0.124 ± 0.115	0.220 ± 0.128
Ocean mean (smoothed)	0.126 ± 0.007	0.115 ± 0.021	0.210 ± 0.019
Land mean (smoothed)	0.182 ± 0.038	0.209 ± 0.043	0.218 ± 0.022
Global mean (smoothed)	0.142 ± 0.015	0.146 ± 0.027	0.216 ± 0.021

Note. The uncertainties are square roots of summations over the squared internal and statistical uncertainties listed in Table 4. Units are in K/decade.

internal uncertainty over land in STAR V5.0 (0.04 K/decade) is close to the total internal uncertainty estimate in Mears et al. (2011), owing to larger uncertainty estimates in diurnal drift adjustment over land.

Also shown in Table 4 are statistical uncertainties associated with the length and variability of a time series in trend calculations. The internal trend uncertainty is different from the statistical uncertainty which would typically be larger but become smaller as observations become longer (Wigley, 2006). This is evidenced in Table 4 when comparing the statistical uncertainties for the period of 1979–2021 (around 0.04 K/decade) to those for the periods of 1979–1996 (around 0.11 K/decade) and 2002–2021 (around 0.12 K/decade).

TMT has a significant weight from the lower stratosphere and its contribution to the TMT trend needs to be corrected to derive the tropospheric temperature trend (Fu & Johanson, 2005; Fu et al., 2004; Spencer & Christy, 1992b; Wentz & Schabel, 2000). The lower stratospheric contribution can be removed by using the lower-stratospheric temperature (TLS) time series observed by the MSU channel 4 (57.95 GHz) (Fu & Johanson, 2005; Fu et al., 2004). Based on the characteristics of their weighting functions, TMT and TLS can be combined together to provide an adjusted mid-tropospheric temperature time series with negligible contribution from the lower-stratosphere (Fu et al., 2004). This combination equation is written as $TTT = a_{24} \times TMT + (1 - a_{24}) \times TLS$, here a_{24} is a regression coefficient and TTT stands for Temperature Total Troposphere, the adjusted TMT measuring the tropospheric layer from the Earth's surface to about 10 km above. For global means, $a_{24} = 1.15$ gives an accurate adjustment for the lower-stratospheric effect (Fu & Johanson, 2005; Fu et al., 2004). Note that even if the TLS trend is zero, the correction of 15% is still needed since TMT only gives 87% weight to the troposphere which needs to be normalized to one to correctly represent the tropospheric temperature.

Table 5 lists the TTT trends for the periods corresponding to Table 4 and Figure 14 shows the anomaly time series of global mean TTT. Here the TLS was also from STAR V5.0 which was developed using the same approach as the STAR V5.0 TMT. The trend uncertainties in Table 5 are square roots of summations over the squared internal and statistical uncertainties. As seen in Table 5, tropospheric warming trends are observed for all three periods and over both land and ocean. For the latest half period, trends over ocean, land and globe were close to each other. Trends over land (0.183 K/decade) was 45% higher than over ocean (0.126 K/decade) for the entire observation period from 1979 to 2021. The global mean TTT trend was 0.142 ± 0.045 K/decade from 1979 to 2021, translating to a total warming of 0.603 K during this period. A striking feature is that trends during the latest half period (around 0.21–0.22 K/decade) nearly doubled the trends during the first half period (around 0.10–0.12 K/decade) for the global and global ocean means. These large differences in TTT trends between the first and second half periods suggest that the tropospheric warming is accelerating.

To estimate the acceleration rate of TTT warming and have the results less sensitive to the selection of separation points between the first and second periods, we smoothed the TTT time series using the locally weighted

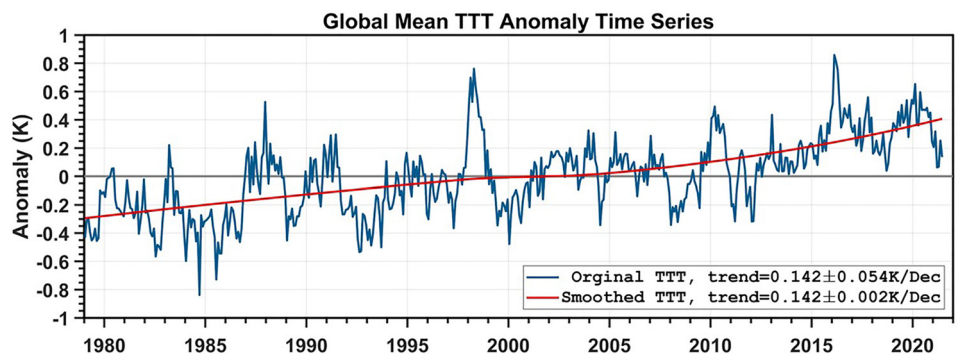

Figure 14. Global mean Temperature Total Troposphere (TTT, TMT adjusted by TLS) time series (blue lines) and its smoothed time series (red lines). The locally weighted regression method (Cleveland, 1979) is used for the smoothing. Both TMT and TLS for TTT generation are from STAR V5.0.

regression method (LOESS, Cleveland, 1979). LOESS is a robust fitting procedure capable of capturing complex nonlinear and multi-modal relationships in time series (Cleveland, 1979; Cleveland & Devlin, 1988). This smoothed TTT for global mean time series is also shown in Figure 14, and Table 5 lists its trends for the three periods of interest to compare with results from the original TTT time series. As seen, the trend of the smoothed TTT was exactly the same as the unsmoothed TTT time series for the entire period, and trend in the latest half period was also nearly doubled the trend in the first half period for ocean means. Since the smoothed TTT does not contain the spikes of 1998 El Nino, the large trend difference between the first and second half periods is robust and is not very sensitive to the selection of the separation points between the two periods. Using trend values in the smoothed TTT in Table 5, the acceleration rate of TTT warming was estimated to be 0.029 K decade^{-2} and 0.039 K decade^{-2} for global and global ocean means, respectively. This would add about 0.5 K additional warming over 50 years compared with linear warming. Richardson (2022) reported an acceleration rate of 0.049 K decade^{-2} for multiple surface temperature data sets used in the Intergovernmental Panel on Climate Change 5th Assessment Report (IPCC, 2014) during 1980–2020, a time period close to our study. When accounting for effects of El Nino, volcanism, and solar activity in the surface time series, the acceleration rate became 0.035 K decade^{-2} (Richardson, 2022). Although with large uncertainties associated with different techniques, the TTT acceleration rate estimated here over the ocean is within the range estimated from the surface temperature data sets.

The above TTT trends have strong implications for trends in climate model simulations and other observations. Santer et al. (2021) reported that the multi-model averages for the TTT trends from CMIP5 and CMIP6 were 0.28–0.29 K/decade during 1979–2019. The total TTT trend found in this study was only one-half of the climate model simulations during the same period. This is consistent with conclusions in McKitrick and Christy (2020) for a slightly shorter period (1979–2014). Possible reasons for the observation-model differences in trends may include climate model biases in responding to external forcings (McKitrick & Christy, 2020), deficiencies in the post-millennium external forcings used in model simulations (Santer, Fyfe, et al., 2017), phase mismatch in natural internal climate variability (Po-Chedley et al., 2021; Suárez-Gutiérrez et al., 2017), and possible residual errors in satellite data sets.

Climate models also maintained a value of 5.3%–5.5% K^{-1} for the ratio of the atmospheric moisture trend over the TTT trend over the tropical ocean, reflecting the fact that the tropical temperature changes closely follow a moist adiabatic lapse rate (Santer et al., 2021). However, the observed moisture trends from satellite microwave imagers were 1.46%/decade over the tropical ocean during 1988–2019 (Santer et al., 2021), resulting in a moisture and temperature trend ratio about 10% K^{-1} when TTT trends over the tropical ocean in this study (0.145 K/decade) was used. This would suggest that satellite-derived moisture trends could be too high. However, it is also possible that trends from our newly developed TTT time series is too low. Afterall, minimizing inter-satellite differences is a necessary but not sufficient condition for the merged time series to accurately detect climate trends. This applies to both the satellite moisture and temperature products. Having a reference time series with high accuracy in trend detection in the merging process in STAR V5.0 increases its chances to detect climate trends with a better accuracy. However, since the reference time series only covers part of the entire observation period, errors in trend detection may still exist for the entire observation period. Further investigation is still needed to resolve the trend accuracy issues with the satellite moisture and temperature products.

9. Conclusion

We have developed STAR V5.0 TMT time series for the period from late 1978 to present using a backward merging approach. The RTMT time series during 2002–present based on AMSU-A and ATMS observations onboard satellites in stable sun-synchronous orbits was used as the reference and earlier satellites before NOAA-19 were adjusted to RTMT in the backward merging. Brightness temperatures from NOAA-10 to NOAA-19 were recalibrated first before they were merged with RTMT and a semi-physical model was developed for diurnal drift adjustment. Adjustments of channel frequency differences between MSU and AMSU-A companion channels and instrument blackbody warm target effects were also conducted on observed radiances. The recalibration and adjustments for diurnal drift and warm target effects had effectively removed satellite bias drifts and resulted in inter-consistent satellite radiance data with small inter-satellite difference trends and standard deviations. Major differences in STAR V5.0 from the existing data sets is that recalibration has removed large spurious warming drifts in NOAA-11, NOAA-12, and NOAA-14 and a large cooling drift in NOAA-15 observations.

The removal of the spurious warming drifts in NOAA-11 to NOAA-14 resulted in the warming trends in STAR V5.0 during 1979–2021 much smaller than the existing versions of the STAR and RSS data sets but close to the latest version of the UAH data set. After removal of the lower-stratospheric cooling effect, the total tropospheric temperature trend derived from TMT was 0.142 ± 0.045 K/decade from 1979 to 2021. This total trend was separated by two distinct periods with trends during the latest half period were nearly doubled the earlier half period over ocean and the globe, showing accelerating tropospheric warming. The estimated acceleration rate of the tropospheric warming was about 0.029–0.39 K decade^{-2} over ocean and the globe.

The STAR V5.0 data set. also include TUT, TLS and TLT time series. Similar backward merging approaches and diurnal adjustment algorithms as used in the TMT development were applied to TUT and TLS channels for their development. TLT is obtained using regressions of TMT, TUT, and TLS following approaches in Spencer et al. (2017).

The STAR V5.0 CDR for TLT, TMT, TUT, and TLS is publicly accessible from the STAR website with a URL address: https://www.star.nesdis.noaa.gov/smcd/emb/mscat/products.php. Plans are also being developed to transition the STAR V5.0 data set to NOAA/NCEI for operational archiving and distribution for user applications.

The cut-off dates for MSU and AMSU-A observations used in STAR V5.0 from all earlier satellites were before the end of 2018. Future update of STAR V5.0 will only need update of the ATMS observations in RTMT. The update of the monthly RTMT has been made every month for ATMS observations onboard SNPP and NOAA-20. Future JPSS satellites such as JPSS-2 are planned to be launched onto the same stable orbits as in SNPP and NOAA-20. When ATMS observations from these satellites are available, they will be simply added to RTMT without the need for diurnal drift adjustment. Such a STAR V5.0 data set is expected to extend to the next 20 years for climate change monitoring and assessment in the atmospheric temperatures.

Appendix A: Recalibration of MSU and AMSU-A Observations Using MetOp-A as a Reference

Recalibration of the MSU and AMSU-A observations in this study is based on the measurement principles for these instruments and a calibration approach developed by Zou et al. (2006, 2009) and Zou and Wang (2011). Specifically, the MSU and AMSU-A calibration relied on two calibration targets as end point references: a cosmic space cold target and an onboard blackbody warm target. The cold space has a temperature of 2.73 K, and the warm target temperature is measured by platinum resistance thermometers (PRTs) embedded in the blackbody target. In each scan cycle, an instrument looks at these two targets, as well as the Earth, and the signals in the form of electric voltage are processed by the instrument and finally converted to digital counts through an analog-to-digital converter. These digital counts were output as raw observations in the MSU and AMSU-A level-1b files. The MSU and AMSU-A level-1 calibration equation (also known as instrument transfer equation) converts the raw counts to radiances using the two calibration targets as follows (e.g., Mo, 1995, 1996; Zou et al., 2006):

$$R_e = R_L + \mu Z \tag{A1}$$

where R_e is the earth scene radiance, $R_L = R_c + G^{-1}(C_e - C_c)$, representing the dominant linear response, and $Z = G^{-2}(C_e - C_c)(C_e - C_w)$ is a quadratic nonlinear response characterizing the non-perfect square law nature of a detector. C represents the raw counts value of the satellite observations and $G = \frac{(C_w - C_c)}{(R_w - R_c)}$ is the instrument gain. The subscripts e, w, and c refer to the earth-view, onboard blackbody warm target view, and cold space view, respectively; and μ is a nonlinear coefficient representing the magnitude of the calibration nonlinearity. The cold space reference temperature is assumed to be 4.78 K for MSU which includes the actual cold-space temperature of 2.73 K plus an increase of about 2 K owing to the antenna sidelobe radiation. For AMSU-A, channel-dependent sidelobe correction taken from prelaunch laboratory measurements was applied to the cold-space temperature (Mo, 1995). Once the nonlinear coefficient is known, radiance is computed through Equation (A1) and the antenna temperature is then computed using the Planck function. Antenna pattern correction is not conducted here since it does not affect trends of the time series. For convenience, the antenna temperature is referred to as the brightness temperature, T_b, throughout this study.

Equation (A1) was the original calibration equation used by NOAA for operational generation of the level-1c radiances where the nonlinear coefficient, μ, was determined from prelaunch laboratory tests (Mo, 1995).

Calibration using prelaunch specified nonlinear coefficient is referred to as operational calibration here. After satellite launch, changes in observation environment and instrument degradation may result in calibration errors. Three types of errors are considered here: the warm target error ΔR_w, the cold space error ΔR_c, and the nonlinearity error $\Delta\mu$. By assuming the counts are free of errors, the calibration biases arising from these errors can be derived from Equation A1,

$$\Delta R_e = \Delta R_c + K(\Delta R_w - \Delta R_c) + \left[\Delta\mu + \frac{2\mu(\Delta R_w - \Delta R_c)}{R_w - R_c}\right] Z, \tag{A2}$$

here $K = \frac{C_e - C_c}{C_w - C_c}$. Since the warm and cold target errors (on the order of 2 K) are much smaller than the difference of the warm target and cold space temperatures (on the order of 300 K), and the nonlinearity error is on the same order as the nonlinearity itself (Zou et al., 2009), the second term in the square brackets can be ignored.

By definition, the K and Z terms have a quadratic relationship, $K(K-1) = Z/(R_w - R_c)^2$. Since C_c is much smaller than C_e and C_e is closer but smaller than C_w, the K values vary between 0.7 and 0.9. In this range, the $K-Z$ relationship is dominated by a linear term plus a weak nonlinear correction, that is, $K \approx a + bZ + cZ^2 + \ldots$, where a, b, and c are constants (the expression can be obtained using a Taylor expansion around $K = a = 0.85$ and $T_w = 280$ K). When higher order terms are ignored and only the linear terms remain in the $K-Z$ relationship, Equation A2 can be written as

$$\Delta R_e = \delta R + \delta\mu Z, \tag{A3}$$

where δR and $\delta\mu$ represent an offset and errors in instrument nonlinearity, expressed respectively as

$$\delta R = a\Delta R_w + (1-a)\,\Delta R_c, \tag{A4}$$

and

$$\delta\mu = \Delta\mu + b(\Delta R_w - \Delta R_c). \tag{A5}$$

Dimensional analysis gives $bZ \sim 0.2$, $\mu Z \sim 2$ K, $(\Delta R_w - \Delta R_c) \sim 2$ K, and thus $b(\Delta R_w - \Delta R_c) \sim 0.2\mu$. Since $\Delta\mu$ is on the same order as μ itself, the second term is small compared to the first term on the right-hand side of Equation A5.

Subtracting Equation A3 from Equation A1, the error free measurement, denoted as $R'_e = R_e - \Delta R_e$, takes the following form,

$$R'_e = R_L - \delta R + (\mu - \delta\mu)Z. \tag{A6}$$

The purpose of our recalibration is to remove or reduce biases and their drifts found in the operational calibration. For this purpose, we assume simple linear time-varying models for the offset and nonlinear coefficient, that is,

$$-\delta R = \delta R_0 + \kappa(t - t_0), \tag{A7}$$

$$\mu - \delta\mu = \mu_0 + \lambda(t - t_1), \tag{A8}$$

where δR_0 and μ_0 are constant offset and nonlinear coefficient, respectively; $\kappa = \boldsymbol{a}\frac{\partial\Delta\boldsymbol{R_w}}{\partial t} + (1-a)\frac{\partial\Delta\boldsymbol{R_c}}{\partial t}$ is the rate of changes in the offset, $\lambda = -\partial\boldsymbol{\delta\mu}/\partial\boldsymbol{t}$ the rate of changes of the nonlinear coefficient, t the time, and t_0 and t_1 the reference times which can be the satellite launch time or any other reference times when the offset and nonlinear coefficient begin to change. Here the time variation of the prelaunch calibration coefficient $\partial\mu/\partial t$ was ignored.

For convenience of discussions in the following, both δR and κ are referred to as target measurement errors and both $\delta\mu$ and λ are referred to as the degradation of instrument nonlinearity. Several possible mechanisms that could cause these errors and degradations are proposed at the end of this Appendix A. Here we first develop an algorithm to obtain the calibration offset δR and nonlinear coefficient $\mu - \delta\mu$. In our recalibration, these calibration coefficients were determined using post-launch simultaneous nadir overpass (SNO) matchups and global ocean mean differences between satellite pairs. The reason for their use in recalibration is that diurnal drifting errors can be ignored in SNOs for all channels and in oceans means for the lower-tropospheric through lower-stratospheric channels (Zou & Wang, 2011). As such, coefficients derived from these matchups could better represent calibration characteristics. Also, using SNOs alone in recalibration cannot determine calibration coefficients for both

satellites in the SNO pairs (Zou et al., 2006, 2009). This is because information on inter-satellite biases in SNOs only allows resolving offset differences between satellite pairs to minimize constant intersatellite biases and their drifts. Similarly, only differences of nonlinear coefficients between satellite pairs can be resolved in SNO regressions to minimize scene temperature dependency in SNO biases. Additional information is needed to resolve the absolute values of nonlinear coefficients in satellite pairs. Christy et al. (2000) found that sun-heating induced intraannual changes in warm target temperature could affect the calibration of T_b. This was referred to as the warm target effect. This effect was most obvious in global ocean mean differences between satellite pairs and was found to serve well for the purpose of obtaining the absolute values of nonlinear coefficients (Zou & Wang, 2011; Zou et al., 2009). The warm target effect and how it is used in our recalibration are further described below.

Combining Equations A6–A8, the radiance differences for the SNO matchups between two satellites are written as

$$\begin{aligned}\Delta R'_e &= R_{L,sat} + \delta R_{0,sat} + k_{sat}(t-t_0) + (\mu_{0,sat} + \lambda_{sat}(t-t_0))Z_{sat} \\ &\quad -\left[R_{L,ref} + \delta R_{0,ref} + k_{ref}(t-t_0) + (\mu_{0,ref} + \lambda_{ref}(t-t_0))Z_{ref}\right] + \varepsilon\end{aligned} \tag{A9}$$

where the subscripts *sat* and *ref* represent the satellite to be recalibrated and the reference satellite, respectively, and ε a residual error due to mismatches in both time and distance in the SNOs. For satellites with orbital drifts, the SNO matchups occurred only over the Polar Regions which are homogenous in space in most cases (Zou et al., 2006). This means they distribute uniformly around the nadir point where the two satellites meet at exactly the same time and location. As a result, the statistical means of ε are zero and thus its effect is ignored in resolving Equation A9 (Zou et al., 2006). Considering that the statistical means of $\Delta R'_e$ should be zero for the SNO matchups, the calibration coefficients, $\delta R_{0,sat}$, k_{sat}, $\mu_{0,sat}$, and λ_{sat}, of the satellite to be recalibrated can be solved by a multi-linear regression of the SNO matchups with known calibration coefficients of the reference satellite. In this study, the AMSU-A on MetOp-A is used as the reference since it achieved an absolutely stability within 0.04 K/decade in the measured brightness temperatures (Zou et al., 2018). In other words, MetOp-A is assumed to be free of calibration drift here, that is, $k_{\mathrm{MetOpA}} = \lambda_{\mathrm{MetOpA}} = 0$. In addition, its constant calibration offset is also assumed to be zero which do not affect satellite merging, that is, $\delta R_{0,\mathrm{MetOpA}} = 0$.

We used an iterative approach developed by Zou et al. (2006) and Zou and Wang (2011) to determine the nonlinear coefficient of the reference satellite, $\mu_{0,\mathrm{MetOpA}}$, and calibration coefficients of the satellite to be recalibrated. This is achieved by conducting a series of sensitivity experiments in which the nonlinear coefficient of the reference satellite was selected at different values within a reasonable range. For each given value, calibration offset and nonlinear coefficient for the other satellite in the pair were obtained from multi-linear regressions of their SNO matchups using Equation A9. For each set of the obtained calibration coefficients, level-1c radiances were generated globally for the satellite pair and inter-satellite T_b difference time series in their global ocean-means were examined. The final determination of the nonlinear coefficient of the reference satellite corresponds to a point when their ocean-mean inter-satellite differences are minimal for the satellite pair. The underlying reason for this approach is that diurnal drift effect is small over ocean for most channels; as a result, the ocean-mean differences reveal warm target effect, or sun-heating induced instrument temperature variability, in radiances that emerges due to inaccurate calibration nonlinearity (Zou & Wang, 2011). Therefore, the iterative approach gives an optimal nonlinear coefficient of the reference satellite that minimizes the warm target effect in the radiances for the recalibrated satellite pair. For the obtained nonlinear coefficients to be of good accuracy, the overlapping periods for the satellite pairs should be long enough to resolve the warm target effect. One-year overlap is a minimal requirement to cover a complete cycle of the instrument temperature variability and to minimize calibration uncertainties due to short overlaps. Furthermore, for the obtained nonlinear coefficient of the reference satellite to be more generic, three satellites including NOAA-15, NOAA-18, and NOAA-19 were recalibrated using the same MetOp-A as the reference. The three satellites all overlapped with MetOp-A for over 8 years (Table 1) and accurate calibration coefficients are expected to be obtained with these long overlaps.

The above algorithm procedure is summarized as follows:

1. For each of the satellites, NOAA-15, NOAA-18, and NOAA-19, first choose a value for $\mu_{0,\mathrm{MetOpA}}$ within (−3, 3) in unit of 10^{-5} (mW) $\left(\mathrm{sr}\cdot\mathrm{m}^2\cdot\mathrm{cm}^{-1}\right)^{-1}$; set $k_{\mathrm{MetOpA}} = 0$, $\lambda_{\mathrm{MetOpA}} = 0$, and $\delta R_{0,\mathrm{MetOpA}} = 0$.
2. Use SNO regressions to obtain $\delta R_{0,sat}$, k_{sat}, $\mu_{0,sat}$, and λ_{sat}, for the satellite;

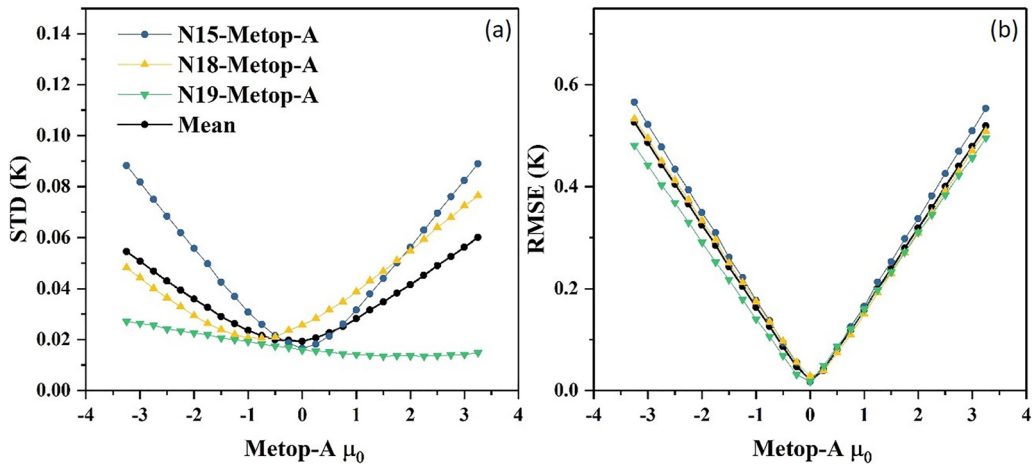

Figure A1. STD (a) and RMSE (b) versus $\mu_{0,\mathrm{MetOpA}}$ for global ocean mean differences of AMSU-A channel 5 between different satellite pairs. The global ocean means are averages of the ascending and descending orbits. The minimums for both the mean STD and mean RMSE occurred at $\mu_{0,\mathrm{MetOpA}} = 0$, which is selected as the final calibration point.

3. Generate level-1c radiances for MetOp-A and the recalibrated satellite using the obtained calibration coefficients;
4. Compute standard deviation of global ocean mean time series of $T_{b,sat}$—$T_{b,\mathrm{MetOpA}}$ for available overlaps between the satellite pairs;
5. Change the value of $\mu_{0,\mathrm{MetOpA}}$ and repeat steps 2, 3 and 4;
6. STOP when a minimal of the standard deviation of ($T_{b,sat}$—$T_{b,ref}$) is found;
7. STOP when all satellites are completed.

By design, the above method gives three optimal calibration coefficients that minimize three types of calibration errors: (a) optimal offset values that minimize constant inter-satellite biases and their linear time-drifts; (b) optimal differences of the nonlinear calibration coefficients between the satellite pairs that minimize scene temperature-dependent biases in the SNO pairs; (c) optimal absolute values of nonlinear coefficients that minimizes the warm target effect in the radiances. Note that by going though both winter and summer, the SNO matchups over the Polar Regions can reach a T_b range of 200–250 K for the MSU channel 2 and AMSU-A channel 5 observations (Zou et al., 2006). This is more than 80% of the global T_b range (200–260 K) for the same channel. Although this is not small, calibration coefficients obtained from the SNO matchups alone still do not cover the entire dynamic range of the measured brightness temperature. However, by allowing $\mu_{0,\mathrm{MetOpA}}$ to vary and selecting its optimal value, the calibration approach provides an additional freedom in the calibration coefficients that have also minimized the global inter-satellite biases. As a result, the final calibration coefficients are applicable to the global T_b range with good accuracy.

Figures A1a and A1b show changes of the Standard Deviation (STD) and Root Mean Square Error (RMSE) of the global ocean mean differences for AMSU-A channel 5 for satellite pairs between the reference MetOp-A and the other three satellites when $\mu_{0,\mathrm{MetOpA}}$ varies within a range around zero. For NOAA-15 and NOAA-18, well defined STD minimums were found close to $\mu_{0,\mathrm{MetOpA}} = 0$. The STD is a quantitative measurement of the warm target effect in the radiances (Zou & Wang, 2011). Minimum STD suggests that the corresponding $\mu_{0,\mathrm{MetOpA}}$ minimizes this effect. However, minimum STD for the NOAA-19 and MetOp-A pair was not found because the instrument temperature-related seasonal variability does not exist in NOAA-19. For average of the three satellite pairs, the minimum STD occurred at $\mu_{0,\mathrm{MetOpA}} = 0$ and this was selected as the best recalibration point. Calibration coefficients for AMSU-A channel 5 corresponding to this point for all the satellites are listed in Table A1. We also recalibrated other AMSU-A channels and their calibration coefficients will be published elsewhere.

Table A1
Calibration Coefficients for AMSU-A Channels 5 and MSU Channel 2 for Different Satellites Obtained From the Recalibration Procedure

	Satellite	δR_0	δR_0(in unit of K)	κ	κ (in unit of K/Dec)	μ_0	λ
AMSU-A Channel 5	Metop-A	0.0	0.0	0.0	0.0	0.0	0.0
	NOAA-15	−0.442	−0.167	0.112	0.423	−1.253	0.126
	NOAA-18	1.056	0.399	−0.071	−0.268	3.083	−0.150
	NOAA-19	0.617	0.233	0.0	0.0	0.752	0.0
MSU Channel 2	NOAA-14	2.136	0.803	−0.118	−0.444	7.156	−0.139
	NOAA-12	1.772	0.666	−0.101	−0.380	6.588	−0.102
	NOAA-11	4.259	1.601	−0.064	−0.241	9.592	−0.047
	NOAA-10	2.841	1.068	−0.018	−0.068	6.513	−0.015
	NOAA-9	2.944	1.106	0.0	0.0	5.971	0.0
	NOAA-8	1.177	0.442	0.0	0.0	7.514	0.0
	NOAA-7	3.021	1.135	0.0	0.0	6.650	0.0
	NOAA-6	2.699	1.015	0.0	0.0	7.375	0.0
	TIROS-N	4.317	1.623	0.0	0.0	5.406	0.0

Note. For simplicity, all δR_0 and μ_0 were adjusted to a reference time of $t_0 = 2001$ and $t_1 = 1998$. Units for $\delta R_0, \mu_0, k$, and λ are 10^{-5} (mW) $\left(\text{sr} \cdot \text{m}^2 \cdot \text{cm}^{-1}\right)^{-1}$, $\left(\text{sr} \cdot \text{m}^2 \cdot \text{cm}^{-1}\right)(\text{mW})^{-1}$, 10^{-5} (mW) $\left(\text{sr} \cdot \text{m}^2 \cdot \text{cm}^{-1}\right)^{-1}(\text{yr})^{-1}$ and $\left(\text{sr} \cdot \text{m}^2 \cdot \text{cm}^{-1}\right)(\text{mW})^{-1}(\text{yr})^{-1}$, respectively. Units for δR_0 and k are also converted to the temperature units of K and K/decade for convenience.

Note that the RMSE minimum occurred at $\mu_{0,\text{MetOpA}} = 0$ for all satellite pairs (Figure A1b). The RMSE contains contribution from both inter-satellite biases and variability between satellite pairs, but the absolute value of the former quantity is much larger than the latter one. As a result, the RMSE largely measures the magnitude of inter-satellite biases. Minimal RMSE indicates that inter-satellite biases are also the smallest, being close to zero actually, for the selected calibration point $\mu_{0,\text{MetOpA}} = 0$. Also note that the time variation of the nonlinear coefficient for NOAA-15 channel 5 is critical for removing its time-varying variability after 2015. Without time variation, the best calibration point gave a STD about 0.03 K (Figure A2). This is 50% larger than the STD value when the NOAA-15 nonlinear coefficient was allowed to change with time (0.02 K, Figure A1a). These results demonstrate that the new calibration coefficients of NOAA-15 are robust in terms of improving its consistency with the reference satellite, MetOp-A.

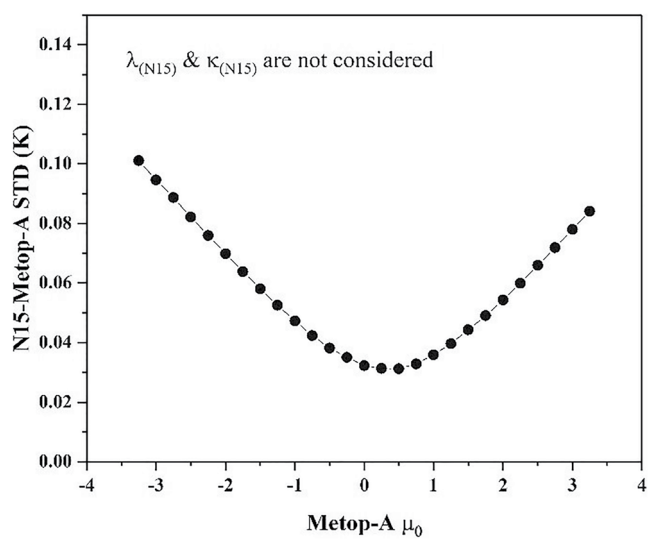

Figure A2. STD versus $\mu_{0,\text{MetOpA}}$ for global ocean mean difference between NOAA-15 and MetOp-A AMSU-A channel 5 when the NOAA-15 nonlinear coefficient are not allowed to change with time.

After recalibration of the AMSU-A instruments, the MSU observations onboard NOAA-10 through NOAA-14 were also recalibrated backward using the recalibrated NOAA-15 as a reference. The same SNO approach as described earlier was applied to obtain the calibration coefficients for the MSU observations. But before the MSU recalibration, the NOAA-14 MSU channels in the SNO matchups were first converted to equivalent AMSU-A channels by applying a frequency adjustment. Similar to the approach as described in Wang and Zou (2014), the simulated differences by the Community Radiative Transfer Model (CRTM, Han et al., 2006) between those with channel frequency inputs taken respectively from AMSU-A and MSU were used as the frequency adjustment to NOAA-14. The simulation was conducted for each SNO event in which the NASA MERRA2 reanalyzes (Gelaro et al., 2017), interpolated to the location and time of SNOs, were used as inputs. After calibration coefficients for NOAA-14 were obtained, NOAA-12 through NOAA-10 were recalibrated using the recalibrated, but without frequency adjusted, NOAA-14 as a reference. Since NOAA-10 and NOAA-9 had only three months of overlaps for MSU channel 2, NOAA-9 through TIROS-N were not recalibrated for this channel. Instead, calibration coefficients for these satellites from previous recalibration studies in Zou and Wang (2010) were still used for MSU channel 2.

The obtained calibration coefficients for MSU channel 2 from NOAA-10 to NOAA-14 are also listed in Table A1. For convenience of discussion, the target measurement errors (δR_0 and κ) are presented in both radiance and equivalent T_b units. As seen, the κ values are 0.42 K/decade for NOAA-15 and range from -0.24 to -0.44 K/decade for NOAA-11 to NOAA-14. We derive the calibration drift budget equation in the following to understand the relative contribution of κ to calibration drifts. Subtracting Equation A6 from Equation A1, taking time derivative on both sides of the equation, and incorporating Equations A7 and A8, we obtain

$$\frac{\partial R_e}{\partial t} - \frac{\partial R'_e}{\partial t} = -\kappa - \lambda Z + [\mu - \mu_0 - \lambda(t - t_1)]\frac{\partial Z}{\partial t} \tag{A10}$$

where the left-hand side of Equation A10 represents drift in operational calibration relative to those after recalibration. This drift was caused by a cancellation effect between the target measurement error (κ) and degradation in nonlinearity (λZ, the multi-year and global mean value of Z is about -0.6×10^{-5} $(\text{mW})^2$ $(\text{sr m}^2\ \text{cm}^{-1})^{-2}$, Zou et al., 2006) with a small adjustment of nonlinear effect (the third term in the right-hand side of Equation A10). With available values for μ_0 and λ in Table A1 and the nonlinear coefficient μ from pre-launch calibration, the contribution from nonlinearity degradation and the small nonlinear effect can be computed. Calibration drift before recalibration was -0.12 K/decade for NOAA-15 (Figure 2a). This was caused by cancellation between the target measurement error of -0.42 K/decade and a total nonlinear effect [summation of the second and third terms in Equation A10] of about 0.3 K/decade. Similarly, calibration drifts before recalibration were about 0.19 K/decade for NOAA-11 to NOAA-14 (Figure 3b). This was caused by a cancellation effect between the target measurement error of 0.24–0.44 K/decade and a total nonlinear effect of 0.05–0.25 K/decade for NOAA-11 to NOAA-14, respectively.

We propose three possible mechanisms for the target measurement errors (κ) and the degradation of nonlinearity (λ). The first one is the sidelobe effect in which the cold space views receive emission from the spacecraft itself. This effect is often expressed as a sidelobe efficiency multiplied by the effective satellite temperatures (Obligis et al., 2007). The sidelobe efficiency ranges from 0.21% to 4.43%, depending on channel frequencies and position of reflectors relative to satellites (Obligis et al., 2007). The sidelobe efficiency could change due to reflector degradation or antenna degradation. For an effective satellite temperature around 190 K (Obligis et al., 2007), a small change on the order of 0.1%–0.2% in the sidelobe efficiency during a decade is large enough to cause a cold target error of 0.19–0.38 K/decade. The second mechanism is a possible change over time in errors in the blackbody radiometric temperature measurements. Instrument calibration generally uses PRT temperatures to represent radiometric temperatures of the blackbody. In reality, however, the blackbody radiometric temperature is proportional to the blackbody emissivity which could vary due to changes in blackbody temperature and surface material. For blackbody temperatures around 300 K, a change of emissivity from 0.9999 to 0.999 during 10 years is large enough to cause a warm target error of 0.27 K/decade. The degradation of warm target emissivity would result in a cooling drift in satellite observations, which was likely the cause for the NOAA-15 cooling drift. On the other hand, the sidelobe effect may result in warming drifts, which was likely the cause for the warming drifts in NOAA-11 to NOAA-14. In reality, both mechanisms could exist on a same satellite as it is their combined effect (κ) that goes into the calibration drift budget equation (Equation A10).

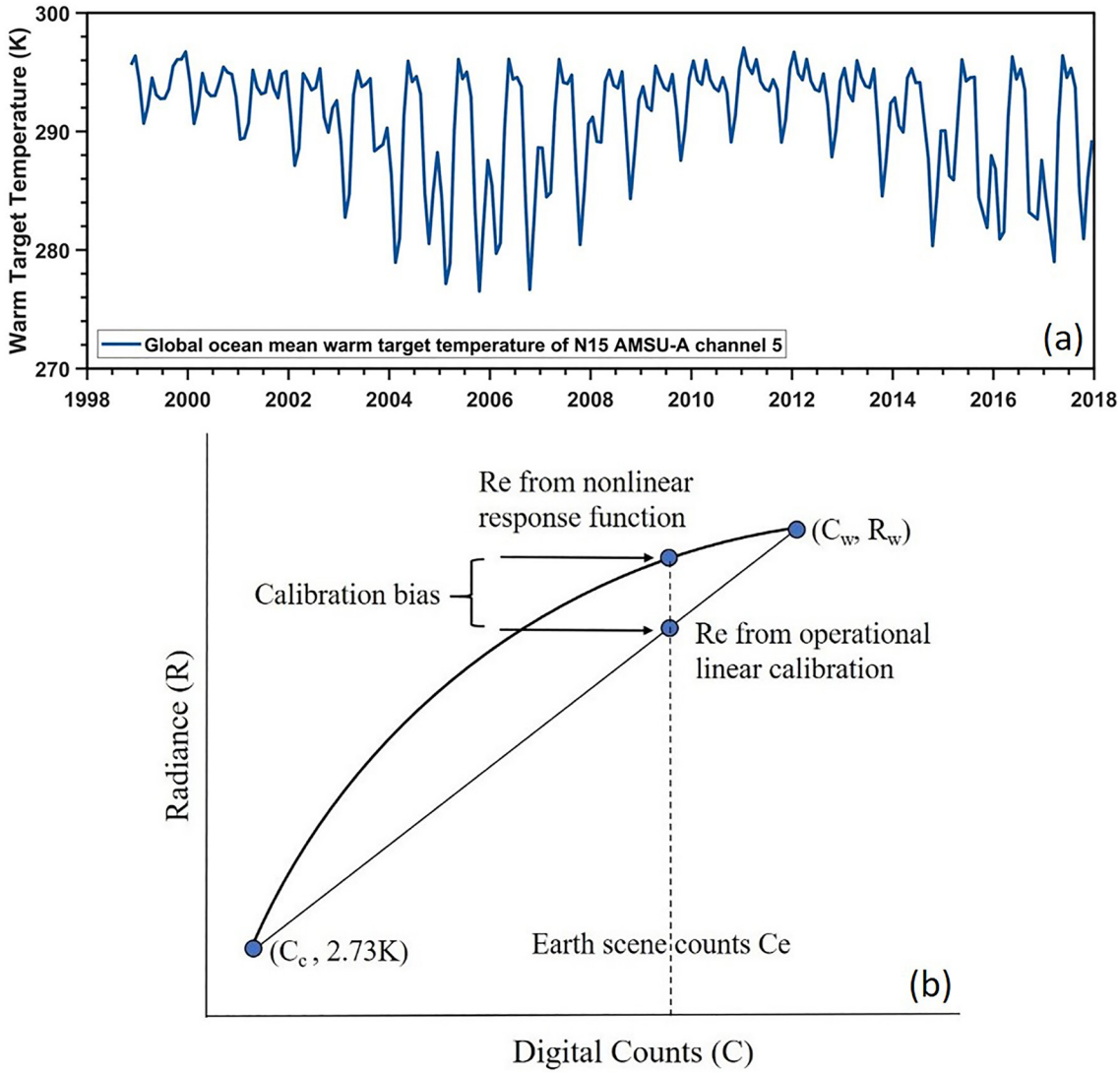

Figure A3. (a) Warm target PRT temperature time series for NOAA-15 AMSU-A channel 5. (b) Schematic shows calibration biases due to degradation of instrument nonlinearity. Here all the symbols are consistent with those in Equation A1.

The third mechanism, degradation in instrument nonlinearity, may include both detector degradation and amplifier degradation. As shown in Equation A10, calibration drifts were partially caused by nonlinearity degradation. Additionally, degradation in nonlinearity also caused warm target effects. As a demonstration, Figure A3a shows warm target temperature time series for NOAA-15 AMSU-A channel 5 and Figure A3b shows a schematic diagram on how nonlinearity degradation would cause a calibration bias. In Figure A3a, large intraannual variability in the warm target temperature time series was observed. This was induced by changes in the angle of incident solar radiation on the satellite (Zou & Wang, 2011). In operational calibration, the nonlinear coefficient estimated from prelaunch laboratory tests was close to zero for NOAA-15 AMSU-A channel 5 (-0.01 to -0.03 in the unit of $\left(\mathrm{sr}\cdot \mathrm{m}^2\cdot \mathrm{cm}^{-1}\right)^{-1}(\mathrm{mW})^{-1}$; Mo, 1995). As a result, the operational calibration can be largely represented by a linear calibration (black thin lines, Figure A3b). With satellite aging, the instrument transfer function could become nonlinear because of degradation in nonlinearity (black thick lines, Figure A3b). This would produce a calibration bias in the operational calibration relative to the actual nonlinear calibration function. This calibration bias could vary with warm target temperature, the so-called warm target effect (Christy et al., 2000). This effect was clearly seen in Figure 2a after 2015 during which large seasonal variability occurred in the difference time series between NOAA-15 and MetOp-A for before NOAA-15 recalibration. With a linear change assumption in the nonlinear coefficient, our recalibration generated a larger nonlinear coefficient after 2015 ($\mu-\delta\mu$ equaled

about 1 in unit of $\left(\mathrm{sr}\cdot \mathrm{m}^2\cdot \mathrm{cm}^{-1}\right)^{-1}(\mathrm{mW})^{-1}$ after 2015). This larger nonlinear coefficient reduced the warm target effect, represented by the standard deviation of the NOAA-15 and MetOp-A difference time series, from 0.048 K for before recalibration to 0.018 K for after recalibration. This was about an 300% improvement in data quality.

Of a final note, although possible mechanisms are proposed here to explain calibration drifts, the calibration coefficients obtained in our recalibration are not restricted to remove biases caused by the proposed mechanisms. This is because calibration coefficients were obtained by data fitting to SNOs and global ocean mean differences following an assumption that time variations of the calibration offsets and nonlinear coefficients are linear. The recalibration procedure and results does not depend on specific mechanisms proposed to explain the errors. The same calibration coefficients would be obtained for other possible mechanisms having similar drifting patterns. Nevertheless, the calibration procedure critically relies on stability of the reference satellite. If the reference satellite (MetOp-A in our case) had a calibration drift, the recalibrated satellites would drift in the same direction as the reference satellite.

Data Availability Statement

The STAR V5.0 CDRs developed in this study are available from the NOAA/STAR website: https://www.star.nesdis.noaa.gov/smcd/emb/mscat/products.php. The reference data sets for TMT, TUT, and TLS used in the STAR V5.0 development are also available from the same NOAA/STAR website. The MSU and AMSU-A L1c data from TIROS-N to NOAA-18 are accessible from the NOAA/NCEI Climate Dara Record Program: https://www.ncei.noaa.gov/products/climate-data-records/fundamental. The NOAA-19 L1b data are available from the NOAA CLASS website: https://www.avl.class.noaa.gov/saa/products/welcome.

Acknowledgments
We thank Dr. Stephen Po-Chedley and another anonymous reviewer for their thoughtful comments that helped improve the manuscript. We also thank Dr. Qiang Fu for helpful discussions during the development of data sets. The work was supported by the NOAA/Joint Polar Satellite System (JPSS) Proving Ground and Risk Reduction (PGRR) Program and NOAA/National Centers for Environmental Information (NCEI) Climate Data Record (CDR) Program. H.X., X.H., & Q. L. were funded by these programs through the NOAA grant NA19NES4320002 (CISESS at the University of Maryland/ESSIC). The views, opinions, and findings contained in this report are those of the authors and should not be construed as an official NOAA or U.S. Government position, policy, or decision.

References

Angevine, W., Edwards, J., Lothon, M., Lemone, M., & Osborne, S. (2020). Transition periods in the diurnally-varying atmospheric boundary layer over land. *Boundary-Layer Meteorology*, *177*(2–3), 205–223. https://doi.org/10.1007/s10546-020-00515-y

Braswell, W. D., & Lindzen, R. S. (1998). Anomalous short wave absorption and atmospheric tides. *Geophysical Research Letters*, *25*(9), 1293–1296. https://doi.org/10.1029/98gl01031

Chapman, S., & Lindzen, R. S. (1970). *Atmospheric tides* (p. 200). D. Reidel.

Chen, H., Zou, X., & Qin, Z. (2018). Effects of diurnal adjustment on biases and trends derived from inter-sensor calibrated AMSU-A data. *Frontiers of Earth Science*, *12*, 1–16. https://doi.org/10.1007/s11707-017-0671-y

Christy, J. R., Spencer, R. W., & Braswell, W. D. (2000). MSU tropospheric temperatures: Dataset construction and radiosonde comparisons. *Journal of Atmospheric and Oceanic Technology*, *17*(9), 1153–1170. https://doi.org/10.1175/1520-0426(2000)017<1153:mttdca>2.0.co;2

Christy, J. R., Spencer, R. W., Braswell, W. D., & Junod, R. (2018). Examination of space-based bulk atmospheric temperatures used in climate research. *International Journal of Remote Sensing*, *39*(11), 3580–3607. https://doi.org/10.1080/01431161.2018.1444293

Christy, J. R., Spencer, R. W., & Lobl, E. S. (1998). Analysis of the merging procedure for the MSU daily temperature time series. *Journal of Climate*, *11*(8), 2016–2041. Retrieved from https://journals.ametsoc.org/view/journals/clim/11/8/1520-0442_1998_011_2016_aotmpf_2.0.co_2.xml

Christy, J. R., Spencer, R. W., Norris, W. B., Braswell, W. D., & Parker, D. E. (2003). Error estimates of version 5.0 of MSU-AMSU bulk atmospheric temperature. *Journal of Atmospheric and Oceanic Technology*, *20*(5), 613–629. https://doi.org/10.1175/1520-0426(2003)20<613:eeovom>2.0.co;2

Cleveland, W. S. (1979). Robust locally weighted regression and smoothing scatterplots. *Journal of the American Statistical Association*, *74*(368), 829–836. https://doi.org/10.2307/2286407

Cleveland, W. S., & Devlin, S. J. (1988). Locally weighted regression: An approach to regression analysis by local fitting. *Journal of the American Statistical Association*, *83*(403), 596–610. https://doi.org/10.2307/2289282

Dai, A., & Wang, J. (1999). Diurnal and semidiurnal tides in global surface pressure fields. *Journal of the Atmospheric Sciences*, *56*(22), 3874–3891. https://doi.org/10.1175/1520-0469(1999)056<3874:dastig>2.0.co;2

Dee, D. P., & Uppala, S. (2009). Variational bias correction of satellite radiance data in the ERA-Interim reanalysis. *Quarterly Journal of the Royal Meteorological Society*, *135*(644), 1830–1841. https://doi.org/10.1002/qj.493

Diamond, H. J., Karl, T. R., Palecki, M. A., Baker, C. B., Bell, J. E., Leeper, R. D., et al. (2013). U.S. Climate Reference Network after one decade of operations: Status and assessment. *Bulletin of the American Meteorological Society*, *94*(4), 489–498. https://doi.org/10.1175/BAMS-D-12-00170.1

Duan, S.-B., Li, Z.-L., Tang, B.-H., Wu, H., Tang, R., Bi, Y., & Zhou, G. (2014). Estimation of diurnal cycle of land surface temperature at high temporal and spatial resolution from clear-sky MODIS data. *Remote Sensing*, *6*(4), 3247–3262. https://doi.org/10.3390/rs6043247

Fu, Q., & Johanson, C. M. (2005). Satellite-derived vertical dependence of tropical tropospheric temperature trends. *Geophysical Research Letters*, *32*(10), L10703. https://doi.org/10.1029/2004GL022266

Fu, Q., Johanson, C. M., Wallace, J. M., & Reichler, T. (2006). Enhanced mid-latitude tropospheric warming in satellite measurements. *Science*, *312*(5777), 1179. https://doi.org/10.1126/science.1125566

Fu, Q., Johanson, C. M., Warren, S. G., & Seidel, D. J. (2004). Contribution of stratospheric cooling to satellite-inferred tropospheric trends. *Nature*, *429*(6987), 55–58. https://doi.org/10.1038/nature02524

Fu, Q., & Lin, P. (2011). Poleward shift of subtropical jets inferred from satellite-observed lower stratospheric temperatures. *Journal of Climate*, *24*(21), 5597–5603. https://doi.org/10.1175/JCLI-D-11-00027.1

Fu, Q., Lin, P., Solomon, S., & Hartmann, D. L. (2015). Observational evidence of strengthening of the Brewer-Dobson circulation since 1980. *Journal of Geophysical Research: Atmospheres*, *120*(19), 10214–10228. https://doi.org/10.1002/2015JD023657

Fu, Q., Manabe, S., & Johanson, C. M. (2011). On the tropical upper tropospheric warming: Models versus observations. *Geophysical Research Letters*, *38*(15), L15704. https://doi.org/10.1029/2011GL048101

Fu, Q., Solomon, S., Pahlavan, H. A., & Lin, P. (2019). Observed changes in Brewer–Dobson circulation for 1980–2018. *Environmental Research Letters*, *14*(11), 114026. https://doi.org/10.1088/1748-9326/ab4de7

GCOS/WMO. (2016). *The Global Observing System for Climate: Implementation needs, GCOS-200 (GOOS-214)* (p. 341). World Meteorological Organization.

Gelaro, R., McCarty, W., Suarez, M. J., Todling, R., Molod, A., Takacs, L., et al. (2017). The Modern-Era Retrospective analysis for Research and Applications, version 2 (MERRA-2). *Journal of Climate*, *30*(14), 5419–5454. https://doi.org/10.1175/jcli-d-16-0758.1

Goldberg, M. D., Crosby, D. S., & Zhou, L. (2001). The limb adjustment of AMSU-A observations: Methodology and validation. *Journal of Applied Meteorology*, *40*(1), 70–83. https://doi.org/10.1175/1520-0450(2001)040<0070:tlaoaa>2.0.co;2

Goldberg, M. D., Kilcoyne, H., Cikanek, H., & Mehta, A. (2013). Joint Polar Satellite System: The United States next generation civilian polar-orbiting environmental satellite system. *Journal of Geophysical Research: Atmospheres*, *118*(24), 13463–13475. https://doi.org/10.1002/2013jd020389

Han, Y., van Delst, P., Liu, Q., Weng, F., Yan, B., Treadon, R., & Derber, J. (2006). *JCSDA community radiative transfer model (CRTM)–Version 1. NOAA Technical Report NESDIS*. (Vol. 122, p. 40). National Oceanic and Atmospheric Administration.

Haurwitz, B., & Cowley, D. (1973). The diurnal and semidiurnal barometric oscillations, global distribution, and annual variation. *Pure and Applied Geophysics*, *102*(1), 193–222. https://doi.org/10.1007/bf00876607

Inamdar, A. K., French, A., Hook, S., Vaughan, G., & Luckett, W. (2008). Land surface temperature retrieval at high spatial and temporal resolutions over the southwestern United States. *Journal of Geophysical Research*, *113*(D7), D07107. https://doi.org/10.1029/2007JD009048

IPCC. (2014). In Core Writing Team, R. K. Pachauri, & L. A. Meyer (Eds.), *Climate Change 2014: Synthesis Report. Contribution of Working Groups I, II and III to the Fifth Assessment Report of the Intergovernmental Panel on Climate Change* (p. 151). IPCC.

Kidwell, K. B. (1998). *NOAA polar orbiter data users guide*. NOAA. Retrieved from http://webapp1.dlib.indiana.edu/virtual_disk_library/index.cgi/4284724/FID2496/podug/index.htm

Kiehl, J. T., Hack, J. J., Bonan, G. B., Boville, B. A., Briegleb, B. P., Williamson, D. L., & Rasch, P. J. (1996). *Description of the NCAR Community Climate Model (CCM3)* (p. 152). National Center for Atmospheric Research Technical Note NCAR/TN-4201STR.

Li, Y., & Smith, R. B. (2010). Observation and theory of the diurnal continental thermal tide. *Journal of the Atmospheric Sciences*, *67*(9), 2752–2765. https://doi.org/10.1175/2010jas3384.1

Lindzen, R. S. (1967). Thermally driven diurnal tide in the atmosphere. *Quarterly Journal of the Royal Meteorological Society*, *93*(395), 18–42. https://doi.org/10.1002/qj.49709339503

Lindzen, R. S. (1978). Effect of daily variations of cumulonimbus activity on the atmospheric semidiurnal tide. *Monthly Weather Review*, *106*(4), 526–533. https://doi.org/10.1175/1520-0493(1978)106<0526:eodvoc>2.0.co;2

McKitrick, R., & Christy, J. R. (2020). Pervasive warming bias in CMIP6 tropospheric layers. *Earth and Space Science*, *7*(9), e2020EA001281. https://doi.org/10.1029/2020ea001281

Mears, C. A., Schabel, M. C., & Wentz, F. J. (2003). A reanalysis of the MSU channel 2 tropospheric temperature record. *Journal of Climate*, *16*(22), 3650–3664. https://doi.org/10.1175/1520-0442(2003)016<3650:arotmc>2.0.co;2

Mears, C. A., & Wentz, F. J. (2009). Construction of the Remote Sensing Systems V3.2 atmospheric temperature records from the MSU and AMSU microwave sounders. *Journal of Atmospheric and Oceanic Technology*, *26*(6), 1040–1056. https://doi.org/10.1175/2008jtecha1176.1

Mears, C. A., & Wentz, F. J. (2016). Sensitivity of satellite-derived tropospheric temperature trends to the diurnal cycle adjustment. *Journal of Climate*, *29*(10), 3629–3646. https://doi.org/10.1175/jcli-d-15-0744.1

Mears, C. A., & Wentz, F. J. (2017). Satellite-derived lower-tropospheric atmospheric temperature dataset using an optimized adjustment for diurnal effects. *Journal of Climate*, *30*(19), 7695–7718. https://doi.org/10.1175/JCLI-D-16-0768.1

Mears, C. A., Wentz, F. J., Thone, P., & Bernie, D. (2011). Assessing uncertainty in estimates of atmospheric temperature changes from MSU and AMSU using a Monte-Carlo estimation technique. *Journal of Geophysical Research*, *116*(D8), D08112. https://doi.org/10.1029/2010jd014954

Mo, T. (1995). *Calibration of the advanced microwave sounding unit-A for NOAA-K, NOAA Technical Report NESDIS 85*. National Oceanic and Atmospheric Administration.

Mo, T. (1996). Prelaunch calibration of the advanced microwave sounding unit-A for NOAA-K. *IEEE Transactions on Microwave Theory and Techniques*, *44*(8), 1460–1469. https://doi.org/10.1109/22.536029

Obligis, E., Eymard, L., & Tran, N. (2007). A new sidelobe correction algorithm for microwave radiometers: Application to the Envisat instrument. *IEEE Transactions on Geoscience and Remote Sensing*, *45*(3), 602–612. https://doi.org/10.1109/tgrs.2006.887165

Ohring, G., Romanov, P., Ferraro, R., Heidinger, A., Laszlo, I., Zou, C.-Z., & Foster, M. (2014). Satellite observations of North American climate change. In *Climate Change in North America* (pp. 95–165). Springer. https://doi.org/10.1007/978-3-319-03768-4_3

Po-Chedley, S., Santer, B. D., Fueglistaler, S., Zelinka, M. D., Cameron-Smith, P. J., Painter, J. F., & Fu, Q. (2021). Natural variability contributes to model-satellite differences in Tropical tropospheric warming. *Proceedings of the National Academy of Sciences of the United States of America*, *118*(13), e2020962118. https://doi.org/10.1073/pnas.2020962118

Po-Chedley, S., Thorsen, T. J., & Fu, Q. (2015). Removing diurnal cycle contamination in satellite derived tropospheric temperatures: Understanding tropical tropospheric trend discrepancies. *Journal of Climate*, *28*(6), 2274–2290. https://doi.org/10.1175/jcli-d-13-00767.1

Randel, W. J., Polvani, L., Wu, F., Kinnison, D. E., Zou, C.-Z., & Mears, C. (2017). Troposphere-stratosphere temperature trends derived from satellite data compared with ensemble simulations from WACCM. *Journal of Geophysical Research: Atmospheres*, *122*(18), 9651–9667. https://doi.org/10.1002/2017JD027158

Richardson, M. T. (2022). Prospects for detecting accelerated global warming. *Geophysical Research Letters*, *49*(2), e2021GL095782. https://doi.org/10.1029/2021GL095782

Robel, J., & Graumann, A. (2014). NOAA KLM user's guide. Retrieved from https://webapp1.dlib.indiana.edu/virtual_disk_library/index.cgi/2790181/FID1497/Klm

Santer, B. D., Fyfe, J. C., Pallottal, G., Flato, G. M., Meehl, G. A., England, M. H., et al. (2017). Causes of differences in model and satellite tropospheric warming rates. *Nature Geoscience*, *10*(7), 478–485. https://doi.org/10.1038/ngeo2973

Santer, B. D., Painter, J. F., Mears, C. A., Doutriaux, C., Caldwell, P., Arblaster, J. M., et al. (2013). Identifying human influences on atmospheric temperature. *Proceedings of the National Academy of Sciences*, *110*(1), 26–33. https://doi.org/10.1073/pnas.1210514109

Santer, B. D., Po-Chedley, S., Feldl, N., Fyfe, J., Fu, Q., Solomon, S., et al. (2022). Robust anthropogenic signal identified in the seasonal cycle of tropospheric temperature. *Journal of Climate*, *35*(18), 6075–6100. https://doi.org/10.1175/JCLI-D-21-0766.1

Santer, B. D., Po-Chedley, S., Mears, C., Fyfe, J. C., Gillett, N., Fu, Q., et al. (2021). Using climate model simulations to constrain observations. *Journal of Climate*, *34*, 6281–6301. https://doi.org/10.1175/JCLI-D-20-0768.1

Santer, B. D., Po-Chedley, S., Zelinka, M., Cvijanovic, I., Bonfils, C., Durack, P., et al. (2018). Human influence on the seasonal cycle of tropospheric temperature. *Science*, *361*(6399), eaas8806. https://doi.org/10.1126/science.aas8806

Santer, B. D., Solomon, S., Pallotta, G., Mears, C., Po-Chedley, S., Fu, Q., et al. (2017). Comparing tropospheric warming in climate models and satellite data. *Journal of Climate*, *30*(1), 373–392. https://doi.org/10.1175/jcli-d-16-0333.1

Santer, B. D., Wigley, T. M., Mears, C., Wentz, F. J., Klein, S. A., Seidel, D. J., et al. (2005). Amplification of surface temperature trends and variability in the tropical atmosphere. *Science*, *309*(5740), 1551–1556. https://doi.org/10.1126/science.1114867

Seidel, D. J., Li, J., Mears, C., Moradi, I., Nash, J., Randel, W. J., et al. (2016). Stratospheric temperature changes during the satellite era. *Journal of Geophysical Research*, *121*(2), 664–681. https://doi.org/10.1002/2015JD024039

Spencer, R. W., & Christy, J. R. (1992a). Precision and radiosonde validation of satellite gridpoint temperature anomalies. Part I: MSU channel 2. *Journal of Climate*, *5*(8), 847–857. https://doi.org/10.1175/1520-0442(1992)005<0847:parvos>2.0.co;2

Spencer, R. W., & Christy, J. R. (1992b). Precision and radiosonde validation of satellite gridpoint temperature anomalies. Part II: Tropospheric retrieval and trends during 1979–90. *Journal of Climate*, *5*(8), 858–866. https://doi.org/10.1175/1520-0442(1992)005<0858:parvos>2.0.co;2

Spencer, R. W., Christy, J. R., & Braswell, W. D. (2017). UAH version 6 global satellite temperature products: Methodology and results. *Asia-Pacific Journal of the Atmospheric Sciences*, *53*(1), 121–130. https://doi.org/10.1007/s13143-017-0010-y

Steiner, A., Ladstädter, F., Randel, W. J., Maycock, A. C., Fu, Q., Claud, C., et al. (2020). Observed temperature changes in the troposphere and stratosphere from 1979 to 2018. *Journal of Climate*, *33*(19), 1865–8194. https://doi.org/10.1175/JCLI-D-19-0998.1

Suárez-Gutiérrez, L., Li, C., Thorne, P. W., & Marotzke, J. (2017). Internal variability in simulated and observed tropical tropospheric temperature trends. *Geophysical Research Letters*, *44*(11), 5709–5719. https://doi.org/10.1002/2017GL073798

Svetunkov, I. (2022). *Forecasting and analytics with ADAM*. *Monograph*. OpenForecast. Retrieved from www.openforecast.org/adam

Trenberth, K. E., & Hurrell, J. W. (1997). How accurate are satellite 'thermometers'? *Nature*, *389*(6649), 342–343. https://doi.org/10.1038/38640-c1

Wang, W., & Zou, C.-Z. (2014). AMSU-A-only atmospheric temperature data records from the lower troposphere to the top of the stratosphere. *Journal of Atmospheric and Oceanic Technology*, *31*(4), 808–825. https://doi.org/10.1175/JTECH-D-13-00134.1

Weng, F., Zou, X., Wang, X., Yang, S., & Goldberg, M. D. (2012). Introduction to Suomi national polar-orbiting partnership advanced technology microwave sounder for numerical weather prediction and tropical cyclone applications. *Journal of Geophysical Research*, *117*(D19), D19112. https://doi.org/10.1029/2012JD018144

Wentz, F. J., & Schabel, M. C. (1998). Effects of satellite orbital decay on satellite-derived lower-tropospheric temperature trends. *Nature*, *394*(6694), 661–664. https://doi.org/10.1038/29267

Wentz, F. J., & Schabel, M. C. (2000). Precise climate monitoring using complementary satellite data sets. *Nature*, *403*(6768), 414–416. https://doi.org/10.1038/35000184

Wigley, T. M. L. (2006). Statistical issues regarding trends. In T. R. Karl, S. J. Hassol, C. D. Miller, & W. L. Murray (Eds.), *Temperature trends in the lower atmosphere: Steps for understanding and reconciling differences*. Retrieved from https://www.globalchange.gov/browse/reports/sap-11-temperature-trends-lower-atmosphere-steps-understanding-reconciling

Zou, C.-Z., Gao, M., & Goldberg, M. (2009). Error structure and atmospheric temperature trends in observations from the microwave sounding unit. *Journal of Climate*, *22*(7), 1661–1681. https://doi.org/10.1175/2008JCLI2233.1

Zou, C.-Z., Goldberg, M., Cheng, Z., Grody, N., Sullivan, J., Cao, C., & Tarpley, D. (2006). Recalibration of microwave sounding unit for climate studies using simultaneous nadir overpasses. *Journal of Geophysical Research*, *111*(D19), D19114. https://doi.org/10.1029/2005JD006798

Zou, C.-Z., Goldberg, M., & Hao, X. (2018). New generation of U.S. satellite microwave sounder achieves high radiometric stability performance for reliable climate change detection. *Science Advances*, *4*(10), eaau0049. https://doi.org/10.1126/sciadv.aau0049

Zou, C.-Z., Li, J., & NCEI. (2015). *NOAA MSU/AMSU-A Mean Layer temperature, Climate Algorithm Theoretical Basis Document (C-ATBD)*. NOAA/NESDIS. Retrieved from https://www.ncei.noaa.gov/pub/data/sds/cdr/CDRs/Mean%20Layer%20Temperatures%20-%20NOAA/AlgorithmDescription_01B-25.pdf

Zou, C.-Z., & Wang, W. (2010). Stability of the MSU-derived atmospheric temperature trend. *Journal of Atmospheric and Oceanic Technology*, *27*(11), 1960–1971. https://doi.org/10.1175/2009JTECHA1333.1

Zou, C.-Z., & Wang, W. (2011). Inter-satellite calibration of AMSU-A observations for weather and climate applications. *Journal of Geophysical Research*, *116*(D23), D23113. https://doi.org/10.1029/2011JD016205

Zou, C.-Z., Xu, H., Hao, X., & Fu, Q. (2021). Post-millennium atmospheric temperature trends observed by satellites on stable orbits. *Geophysical Research Letters*, *48*(13), e2021GL093291. https://doi.org/10.1029/2021GL093291

Zou, X., Weng, F., & Yang, H. (2014). Connecting the time series of microwave sounding observations from AMSU to ATMS for long-term monitoring of climate. *Journal of Atmospheric and Oceanic Technology*, *31*(10), 2206–2222. https://doi.org/10.1175/jtech-d-13-00232.1